Monthly Notices
of the
ROYAL ASTRONOMICAL SOCIETY

MNRAS **468,** 272–290 (2017)
Advance Access publication 2017 February 14

doi:10.1093/mnras/stx373

The population of planetary nebulae near the Galactic Centre: chemical abundances

O. Cavichia,[1,2]★ R. D. D. Costa,[2]★ W. J. Maciel[2] and M. Mollá[3]

[1]*Instituto de Física e Química, Universidade Federal de Itajubá, Av. BPS, 1303, 37500-903 Itajubá-MG, Brazil*
[2]*Instituto de Astronomia, Geofísica e Ciências Atmosféricas, Universidade de São Paulo, 05508-900 São Paulo-SP, Brazil*
[3]*Departamento de Investigación Básica, CIEMAT, Avda. Complutense 40, E-28040 Madrid, Spain*

Accepted 2017 February 9. Received 2017 February 9; in original form 2016 September 16

ABSTRACT

Planetary nebulae (PNe) constitute an important tool to study the chemical evolution of the Milky Way and other galaxies, probing the nucleosynthesis processes, abundance gradients and the chemical enrichment of the interstellar medium. In particular, Galactic bulge PNe (GBPNe) have been extensively used in the literature to study the chemical properties of this Galactic structure. However, the presently available GBPN chemical composition studies are strongly biased, since they were focused on brighter objects, predominantly located in Galactic regions of low interstellar reddening. In this work, we report physical parameters and abundances derived for a sample of 17 high-extinction PNe located in the inner 2° of the Galactic bulge, based on low-dispersion spectroscopy secured at the Southern Astrophysical Research telescope using the Goodman spectrograph. The new data allow us to extend our data base including faint objects, providing chemical compositions for PNe located in this region of the bulge and an estimation for the masses of their progenitors to explore the chemical enrichment history of the central region of the Galactic bulge. The results show that there is an enhancement in the N/O abundance ratio in the Galactic Centre PNe compared with PNe located in the outer regions of the Galactic bulge. This may indicate recent episodes of star formation occurring near the Galactic Centre.

Key words: Galaxy: abundances – Galaxy: bulge – Galaxy: disc – Galaxy: evolution – Galaxy: formation.

1 INTRODUCTION

Planetary nebulae (PNe) are the offspring of stars with a large interval of mass (1–8 $M_{\odot}$). Since they are formed from several different stellar evolutionary pathways (Frew & Parker 2010), they have very heterogeneous intrinsic and observed properties. Also, due to their nature, PNe have a very short lifetime dissipating into the interstellar medium (ISM) in a time-scale of 3–7 $\times$ 10^4 yr (Zijlstra & Pottasch 1991). PNe constitute an important tool to study the chemical evolution of the Milky Way and other galaxies, probing the nucleosynthesis processes, abundances gradients and the chemical enrichment of the ISM. They provide accurate abundance determinations of several chemical elements difficult to study in stars, such as He and N, and also others, such as O, S, Ar and Ne. The former have abundances modified by the evolution of the PN progenitor stars, while the latter reflect the conditions of the ISM at the time the progenitors were formed, although a small depletion of O may be observed due to ON cycling for the more massive progenitors (Clayton 1968), in amounts that depend on metallicity and other properties. Recently, Ne has also been suspected of undergoing self-contamination and its role as a metallicity tracer for the ISM is also uncertain (Milingo et al. 2010).

The currently known number of Galactic bulge planetary nebulae (GBPNe) is ∼800 after the publication of the two Macquire/AAO/Strasbourg Hα PN surveys (Parker et al. 2006; Miszalski et al. 2008). This number is low compared with the estimated numbers of ∼2000 GBPNe by Gesicki et al. (2014) and ∼3500 GBPNe by Peyaud et al. (2006). The currently known number of GBPNe with accurate chemical abundances is ∼300, considering the works done by Escudero & Costa (2001), Escudero, Costa & Maciel (2004), Cavichia, Costa & Maciel (2010), IAG-USP sample, and also the works of Górny et al. (2009), Wang & Liu (2007), Cuisinier et al. (2000), Exter, Barlow & Walton (2004), as compiled by Chiappini et al. (2009). The fact that the PNe are the products of stars of different masses and, consequently, evolutionary pathways, hampers the construction of representative samples for unbiased chemical composition studies.

★ E-mail: cavichia@unifei.edu.br (OC); roberto.costa@iag.usp.br (RDDC)

The presently available chemical composition studies are strongly biased since they focused on brighter objects, predominantly located in Galactic regions of low interstellar reddening. The principal obstacle in deriving accurate chemical abundances towards the Galactic Centre (GC) is the very high level of extinction close to the Galactic plane, where the interstellar extinction caused by the Galactic disc dust layers can reach $A_V \sim 25$ mag (Gonzalez et al. 2012). However, it is precisely in the region close to the GC, where a large fraction of the PN population is expected to exist (Jacoby & Van de Steene 2004, hereafter JS04). The chemical abundance distributions of GBPNe in the bulge region within 2° of the GC is poorly known, as shown in fig. 2 of Chiappini et al. (2009). The discovery of 160 GBPNe near the GC by JS04 opens the possibility to overcome this bias in the chemical abundance studies. This sample is relatively large, covering nearly two-thirds of the predicted number of GBPNe expected in the surveyed region of the Galactic bulge. Thanks to the access to larger telescopes, now it is possible to secure chemical abundance analysis of this high-extinction and low surface brightness GBPNe.

GBPNe near the GC are especially important since they can shed light on the more general problem of the bulge formation and evolution. For instance, GBPNe can contribute to understand what type of collapse formed the bulge (dissipational or dissipationless), and the role of the secular evolution within the Galaxy. The latter can be probed by GBPNe near the GC since the secular evolution causes a significant amount of star formation within the centre of galaxies (Ellison et al. 2011), rejuvenating the stellar populations near the central parsecs of these galaxies (Coelho & Gadotti 2011). If the Galactic bulge is a classical one, then it is formed by gravitational collapse (Eggen, Lynden-Bell & Sandage 1962) or by hierarchical merging of smaller objects and the corresponding dissipative gas process (Zinn 1985). In this case, the formation process is generally fast and occurs earlier in the Galaxy formation process, before the present disc was formed. On the contrary, if the Galactic bulge is formed by the rearrangement of the disc material, it should be constituted by stellar populations that are similar to those of the inner disc.

A complete survey of the abundances of all known GBPNe is currently beyond our capabilities and we need to observe smaller samples, as in this work, to achieve a more statistically complete coverage of the chemical properties of the intermediate-mass population of the bulge. These results would have a significant impact on Galactic evolution theories, providing a much more accurate view of the abundance distribution of GBPNe, especially in the region within 2° of the GC and, therefore, producing more reliable constraints for the modelling of intermediate-mass stars evolution as well as the chemical evolution of the Galactic disc and bulge. In particular, follow-up spectroscopy of GBPNe can tell us the rate at which the alpha elements were enhanced near the GC. In this paper, for the first time, we report spectroscopic follow-up observations of a sample of GBPNe within a few degrees of the GC. These new data provide chemical composition for PNe located in this region of the bulge and an estimation for the masses of their progenitors to explore the chemical enrichment history of the central region of the Galactic bulge. This paper is organized as follows. Section 2 describes the criteria for sample selection, the observations and the data reduction. Section 3 presents the determination of the physical conditions and the ionic and total abundances of our targets. Section 4 is devoted to the data analysis and the comparison of the results obtained in this paper with other results in the literature. Section 5 summarizes the main findings of this work.

2 SAMPLE SELECTION, OBSERVATIONS AND DATA REDUCTION

2.1 Sample selection and bulge membership

The GBPN population in this work was selected mainly from the catalogue of JS04. In this catalogue, the positions, angular diameters, Hα +[N II] fluxes and 5 GHz fluxes are given for a sample of 94 GBPNe. This survey uses a narrow-band imaging in the near-IR [S III] line at 9532 Å to detect high-extinction GBPNe since this line is the apparently brightest line in the spectra of typical PNe when the *V*-band extinction is between 4 and 12 mag. This point will be addressed in more detail in Section 2.2, where the spectra of the GBPNe of our sample will be presented. JS04 estimated that their survey identified nearly two-thirds of the predicted total number of PNe within 2° from the GC.

Usually, GBPNe are selected following the standard criteria of Stasińska, Richer & McCall (1998): they have locations within 10° of the GC, diameters smaller than 12 arcsec and fluxes at 5 GHz lower than 100 mJy. The combination of these criteria leads to the rejection of about 90–95 per cent of foreground disc PNe that are in the direction of the Galactic bulge. In this paper, these criteria were used whenever possible to select GBPNe from the sample of JS04. Although these criteria may reject some true extended GBPNe, these objects are very difficult to be detected in the surveys and, in case of detection, they are extremely faint to provide accurate fluxes for chemical abundances determinations. Additionally from the sample of JS04, we also observed four objects from the catalogue of Parker et al. (2006), which are included in our analysis presented in this work. We performed spectroscopic follow-up of 33 objects located within 2° of the GC, in a region of a very high level of reddening. From those objects, 17 had spectra with acceptable quality to derive physical parameters and chemical abundances. In this paper, we present the spectra, physical parameters and chemical abundances for these 17 objects. The longitude–latitude distribution of the sample of GBPNe presented in this work is shown in Fig. 1. In the same figure, the distribution of the data from Cavichia et al. (2010, hereafter CCM10) is shown for comparison. Clearly, the present sample is located in a region much closer to the GC than our previous observations of the Galactic bulge. It is important to note that, to our knowledge, the present sample of GBPNe is the closest sample to the GC than any previous study of chemical composition of GBPNe.

In order to check the bulge membership of our observed sample, we have calculated individual distances for these objects using the statistical distance scale of Stanghellini, Shaw & Villaver (2008) and the data provided by JS04 for the optical angular diameters and fluxes at 5 GHz. Optical diameters were also taken from Parker et al. (2006) for the PPA PNe. The statistical distances may present large errors when used individually, and in some cases they are as high as 30 per cent (Stanghellini et al. 2008). However, when applied to a larger number of objects, they can be very useful to probe the chemical evolution of the Galaxy, as can be seen in Maciel, Lago & Costa (2006), Henry et al. (2010), Cavichia, Costa & Maciel (2011) and references therein. The logarithmic extinctions at Hβ, necessary to derive the distances, were calculated from the fluxes obtained from our own observations. When the fluxes at 5 GHz were not available, equation 6 provided by Cahn, Kaler & Stanghellini (1992) was used to derive equivalent 5 GHz flux from the Hβ flux. In Table 1, columns 1 and 2 list the PNG numbers and the PN names, and column 3 the flux in 5 GHz when available or the equivalent flux derived from the Hβ flux. Column 4 of Table 1 shows the optical

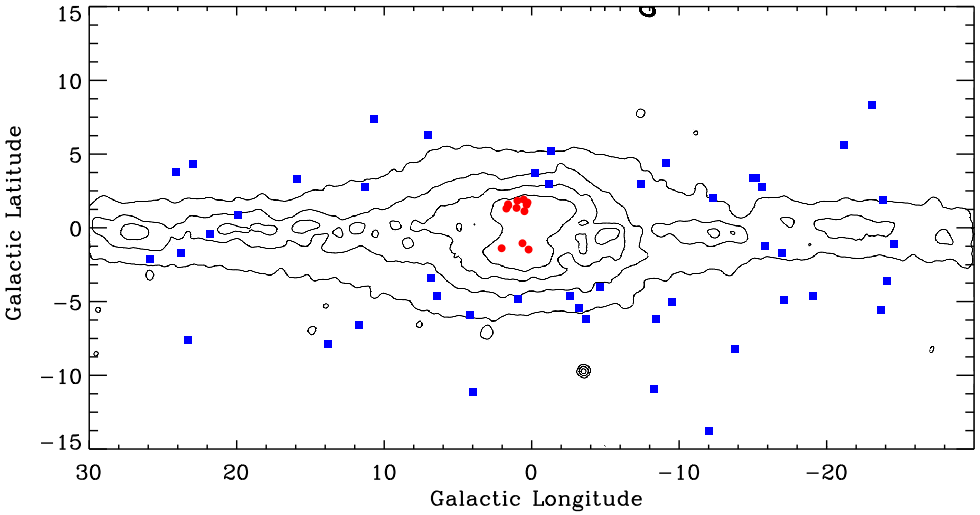

Figure 1. The longitude–latitude distribution of the GBPNe from this work (filled red circles) and the data from CCM10 (filled blue squares). The figure also shows the contours of the COBE/DIRBE 2.2 μm image from Weiland et al. (1994). Note that only GBPNe from this work with abundances listed in Table 9 are included in this figure.

Table 1. Individual galactocentric distances for GBPNe.

PNG	Name	F (mJy)	τ	θ (arcsec)	R (kpc)
0.344 + 1.567[a]	JaSt 23	3	4.079	3.1	−2.19
000.2 + 01.7	JaSt 19	6	3.724	3.1	−0.69
000.2 − 01.4	JaSt 79	4	3.785	2.5	−2.69
000.4 + 01.1	JaSt 36	31	2.906	2.5	0.88
000.5 + 01.9	JaSt 17	10	3.806	4.1	1.28
000.6 − 01.0	JaSt 77	49	3.309	5.1	3.72
000.9 + 01.8	PPA J1740−2708	23	3.192	3.1	1.25
001.0 + 01.3	JaSt 41	16	3.467	3.5	1.42
001.5 + 01.5	JaSt 46	20	3.238	3.1	1.11
001.7 + 01.3	JaSt 52	24	3.017	2.5	0.54
002.0 − 01.3	JaSt 98	21	3.059	2.5	0.41
004.3−01.4	PPA J1801−2553	3	3.955	2.7	−2.48
357.7 + 01.4	PPA J1734−3004	9	3.843	4.1	1.16
358.5 − 01.7	JaSt 64	28	2.946	2.5	0.77
358.9 − 01.5	JaSt 65	122	2.308	2.5	2.59
359.5 − 01.2	JaSt 66	65	2.584	2.5	1.86
359.9 + 01.8	PPA J1738−2800	0	4.472	2.2	−9.25

[a]OH 0.344 +1.567.

thickness parameter, as defined by equation 2 of Stanghellini et al. (2008), and column 5 the optical radius, in arcsec, from JS04 and from Parker et al. (2006). The Galactocentric distances obtained from this method are presented in column 6. Recent estimates for the Galactocentric distance of the Sun (R_0) ranges from 7.5 to 8.5 kpc, and we have adopted the average value R_0 of 8.0 kpc, as suggested by Malkin (2013). In Table 1, the minus sign in the distances indicates the cases when the distances are greater than 8.0 kpc from the Sun. Fig. 2 shows the galactocentric distance distribution for our sample. The Gaussian fitted to the distribution has mean and standard deviation of 0.89 and 0.92 kpc, respectively. Considering the distance of R_0 adopted, the GBPNe studied in this work are ∼0.9 kpc on average from the GC. Therefore, we are very confident that the present sample is composed by bona fide PNe near the GC. However, for all but one object (JaSt 23) the velocity data are not available in the literature and, since the inner disc can extend into the inner kpc of the Galaxy (see a revision by Bland-Hawthorn

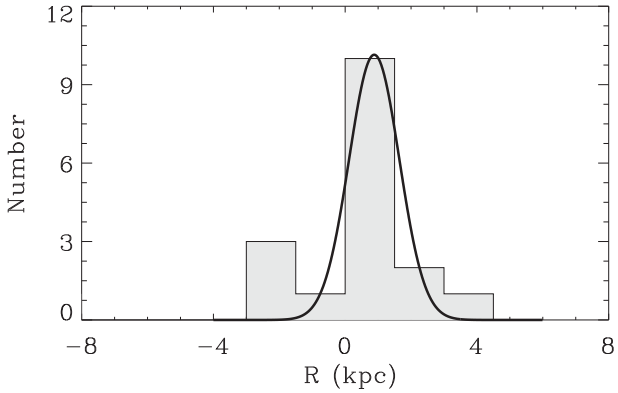

Figure 2. Galactocentric distance distribution for the GBPNe from our sample. The continuous line is the result of the histogram data fitted by a Gaussian with mean and standard deviation of 0.89 and 0.92 kpc, respectively.

& Gerhard 2016), we cannot rule out inner disc PN contaminants in our sample. In the case of JaSt 23, the OH maser spectrum shows a single peak at $V_{\rm LSR} = +115.2\,{\rm km\,s^{-1}}$ (Uscanga et al. 2012), which is compatible with that expected for GBPNe.

2.2 Observations and data reduction

2.2.1 Optical data

In 2009, we started an observational programme aimed at carrying out a spectroscopic follow-up of GBPNe located within 2° of the GC. The 4.1-m SOAR (Southern Astrophysical Research) telescope at Cerro Pachón (Chile) equipped with the Goodman spectrograph was used for this purpose. The long-slit spectra were obtained during the years 2010, 2011 and 2012 using three different volume-phase holographic (VPH) gratings 300, 600 and 400 l mm^{-1}, respectively. In Table 2, we list the VPH gratings, slits, wavelength coverage and the full width at half-maximum (FWHM) resolution achieved for the optical and near-infrared (NIR) observations (see Section 2.2.2). The log of the observations is presented in Table 3, which is described as follows: the PNG number

Table 2. Instrumental setup for optical and NIR observations.

Grating (l mm^{-1})	Slit width (arcsec)	Coverage (Å)	FWHM (Å)
	Optical		
300	1.35	3600–8800	11.8
400	1.68	4000–8050	11.2
600	1.68	4700–7360	7.3
	NIR		
300	2.50	6010–11 010	9.0

(column 1), the name of the object (column 2), the coordinates RA and DEC (columns 3 and 4, respectively), the Galactic longitude and latitude (columns 5 and 6, respectively), the exposition time in seconds (column 7) and the date of observation (column 8). Column 9 lists the VPH grating used in each observation. Columns 10 and 11 list the log of the NIR observations (see Section 2.2.2).

The Goodman spectrograph focal plane is imaged on to a Fairchild 4096 × 4096 pixels CCD with a read rate of 100 kHz. The exposition times varied between 1800 and 2600 s, depending on the faintness of the object. Seeing conditions were in general very good (0.5–0.9 arcsec). For each night, at least two spectroscopic standard stars were observed, through a 3 arcsec wide slit, for flux calibration. Frames containing the same spectral data were combined in order to increase the final signal-to-noise (S/N) ratio. The data were reduced with standard procedures by using an IRAF package developed by our group, the PNPACK. This package automatically reduces long-slit spectra by doing bias subtraction, flat-field correction, extraction of one-dimensional spectra, wavelength calibration, atmospheric extinction correction and flux calibration. Cosmic rays were removed using the algorithm for cosmic ray rejection by Laplacian edge detection (van Dokkum 2001), implemented in the program L.A.Cosmic. In the case of PN spectra, many lines of the observed spectra are weak and, since the objects are located in crowded Galactic bulge fields near the GC, a multistep method had to be adopted to perform the one-dimensional spectra extraction. The best fitting of the background was achieved after removing sky continuum emissions, telluric and interstellar lines, as well as stellar continuum components. The nebular lines were detected and the line fluxes were calculated following an automatic procedure implemented in the PNPACK code. This procedure uses the IRAF task *splot* to perform Gaussian fit to emission lines in the spectra and a Gaussian deblending routine to deblend lines when necessary. Following this procedure, signal can be attributed to a nebular line only if its value is higher than 2σ of the averaged background noise.

2.2.2 *Near-infrared data*

The optical spectra of the GBPNe near the GC suffer for high level of extinction caused by the material near the Galactic plane and also in the central regions of the Galaxy. As a result, important diagnostic lines such as [O III] 4363 Å and [N II] 5755 Å do not have enough S/N ratio to obtain the electron temperature from the temperature diagnostic diagrams. Other important temperature-sensitive lines are those from S^{+3}. The [S III] auroral line at 6312 Å is presented in most of our optical spectra. However, the other two [S III] lines necessary to obtain the electron temperature are NIR lines at 9069 and 9532 Å.

In order to observe the NIR [S III] lines, we started an observational programme in 2012 at the Observatório Pico dos Dias (OPD) of National Laboratory for Astrophysics (LNA, Brazil) with the 1.6-m Perkin-Elmer telescope. The spectrophotometry observations were taken according to the log of observations showed in the last two columns of Table 3. A Cassegrain Boller and Chivens spectrograph was used with a 300 l mm^{-1} grid, which provides a reciprocal dispersion of 0.22 nm pixel^{-1}. An Andor Ikon CCD optimized for NIR observations was used with an operating image scale of 0.56 arcsec pix^{-1} and a pixel size of 13.5×13.5 µm. The science spectra were taken with a long slit of 2.5 arcsec with an FWHM spectral resolution of ∼9 Å. In Table 2, we also list the setup for the NIR observations. Each night at least two of the spectrophotometric standard stars CD-32 9927, LTT 7379, LTT 9239, CD-34 241 of Hamuy et al. (1992, 1994) were observed to improve the flux calibration. These stars were observed with a long slit of 7.5 arcsec width, allowing a more precise flux calibration. Helium–argon arcs were taken immediately after each science spectra in order to perform wavelength calibration. Telluric corrections were not performed since [S III] 9069 and 9532 Å are relatively very intense

Table 3. Log of the observations.

PNG	Name	RA (J2000)	DEC (J2000)	ℓ(°)	b(°)	T_{exp} (s)	Date	Grating	T_{exp} (s) [a]	Date [a]
0.344+1.567[b]	JaSt 23	17 40 23.32	−27 49 11.7	0.35	1.57	2400	Jun 28, 11	600	2400	Jun 26, 12
000.2+01.7	JaSt 19	17 39 39.38	−27 47 22.58	0.28	1.72	2400	Jun 24, 12	300	1800	Jun 26, 14
000.2 − 01.4	JaSt 79	17 51 53.63	−29 30 53.41	0.21	−1.47	2400	Jun 08, 10	300	2400	Jun 26, 12
000.4+01.1	JaSt 36	17 42 25.20	−27 55 36.36	0.49	1.13	2400	Jun 24, 12	300	2400	Jun 25, 12
000.5+01.9	JaSt 17	17 39 31.22	−27 27 46.77	0.55	1.91	2400	Jun 28, 11	600	2400	Jun 27, 12
000.6 − 01.0	JaSt 77	17 51 11.65	−28 56 27.20	0.63	−1.05	1200	Jun 07, 10	300	600	Jun 26, 14
000.9+01.8	PPA J1740−2708	17 40 50.70	−27 08 48.00	0.97	1.84	600	Jun 23, 12	400	–	–
001.0+01.3	JaSt 41	17 42 49.96	−27 21 19.68	1.03	1.35	2400	Jun 08, 10	300	1800	Jun 25, 12
001.5+01.5	JaSt 46	17 43 30.43	−26 47 32.30	1.58	1.52	2400	Jun 28, 11	600	900	Jun 27, 12
001.7+01.3	JaSt 52	17 44 37.30	−26 47 25.23	1.72	1.31	1×300 1×2400	Jun 08, 10	300	1200	Jun 25, 14
002.0 − 01.3	Jast 98	17 55 46.39	−27 53 38.90	2.04	−1.38	2400	Jun 08, 12	400	2400	Jun 26, 12
357.7+1.4	PPA J1734−3004	17 34 46.6	−30 04 21	357.78	1.40	2600	Jun 08, 12	400	–	–
358.5 − 01.7	JaSt 64	17 48 56.04	−31 06 41.95	358.51	−1.74	2×900	Jun 07, 10	300	1800	Jun 25, 14
358.9 − 01.5	JaSt 65	17 49 20.02	−30 36 05.57	358.99	−1.55	1800	Jun 07, 10	300	2400	Jun 26, 12
359.5 − 01.2	JaSt 66	17 49 22.10	−29 59 27.00	359.52	−1.24	2400	Jun 27, 11	600	2400	Jun 26, 12
359.9+01.8	PPA J1738−2800	17 38 11.80	−28 00 07.00	359.93	1.88	2400	Jun 24, 12	400	–	–

[a] Near-infrared observations.
[b] OH 0.3447+1.5656.

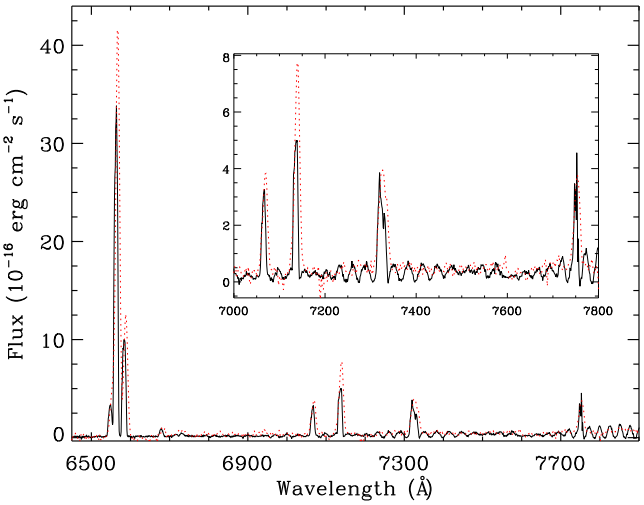

Figure 3. Calibrated optical (black continuous line) and NIR (dashed red line) spectra for JaSt 98 in the region where the line ratios were used to calculate the normalizing constant. In the top-right panel, a zoom in of the faintest lines is shown.

and telluric absorption effects are negligible for these lines. This point will be addressed again in Section 2.2.3, where the observed relative fluxes of these lines are confronted with the expected theoretical values. Data reduction was performed using the IRAF package, following the standard procedure for long-slit spectra, as in the previous section: correction of bias, flat-field, extraction, wavelength and flux calibration. Atmospheric extinction was corrected through mean coefficients derived for the LNA observatory.

The NIR spectra were normalized to match their optical counterparts using as many lines as available in the spectra. The normalizing constant for each NIR spectra was obtained by the flux-weighted mean of the ratio between the NIR line and the optical counterpart. In general, the concordance in flux was good between both spectra (optical and NIR), and the mean ratio of the lines varied between 0.7 and 1.7. The variation of the normalizing constant can be attributed to some causes: atmospheric extinction correction, as we are using the mean extinction absorption coefficients provided by the observatories; the slit widths are different in the optical and NIR observations and this can cause some fluxes loss; cirrus clouds can cause a grey extinction in the spectra and, therefore, change the absolute flux values. In Fig. 3, an example is presented showing the match between the optical and NIR spectra in the region where there are common lines in both observations. In this figure, it is important to note that due to the different instrumental set-ups in both observations, the line profiles are different and the peaks of the lines may not match. The final spectra calibrated in flux and wavelength are shown in Fig. 4. Note that in this figure, the spectra were not corrected for interstellar extinction. The reddened fluxes of the GBPNe are listed in Table 4. In this table, the fluxes are presented relative to the one from the H β line. The errors associated with the fluxes were attributed based on the intensity of the line, as explained in Section 3.4.

2.2.3 *Reddening correction*

To perform a good interstellar extinction correction is crucial for high-extinction GBPNe. As pointed out by Nataf et al. (2013), for most of the bulge, $A_V \approx 2$ is typical. However, for some regions close to the GC, $A_V \approx 50$. The extinction towards the bulge is not only high but also non-standard. The standard value of R_V (the ratio of the total A_V to selective $E(B-V)$ extinction at V) is 3.1 (Fitzpatrick 1999). However, Nataf et al. (2013) found that the optical and NIR reddening law towards the inner Galaxy approximately follows an $R_V \approx 2.5$ extinction curve. On the other hand, Nataf et al. (2016) combined four measures of extinction in the bandpasses $VIJK_s$ and observed that there is no compatibility between bulge extinction coefficients and literature extinction coefficients using any extinction parametrization available (e.g. Cardelli, Clayton & Mathis 1989; Fitzpatrick 1999). Fig. 5 shows a comparison between the extinction curves from Fitzpatrick (1999) in the cases of $R \equiv A(V)/E(B-V) = 3.1$ and 2.5 (black continuous line and red open circles, respectively). The dashed line represents the seventh-degree polynomial fit for $R = 2.5$. The coefficients of the parametrized extinction curve are shown in Table 5. In the same figure, we show for comparison the NIR extinction curve parametrization from Fitzpatrick & Massa (2009) using $R_V = 2.64$ and $\alpha = 2.49$ (see their work for details). Differences between both parametrizations are noted for $\lambda > 1\,\mu$m. Since the most NIR line in our data is the [S III] λ9532 line, we do not expect meaningful variations in the extinction-corrected lines using both parametrizations. In fact, we estimated a difference of $\sim$1 per cent in our approach compared with the NIR parametrization of Fitzpatrick & Massa (2009) at 9532 Å. Therefore, given the uncertainty in the literature with respect to the NIR ($\lambda > 7500$ Å) extinction, we opted to use the Fitzpatrick (1999) extinction parametrization with $R_V = 2.5$, instead of using any of the NIR parametrization provided in the literature.

Our package PNPACK is also able to perform interstellar reddening correction using both extinction curves of Cardelli et al. (1989) and Fitzpatrick (1999). As explained above, in this work we adopted the later extinction curve since it has been shown that it produces better results than the extinction curve of Cardelli et al. (1989) for GBPNe (see e.g. Escudero et al. 2004, for a discussion). The Fitzpatrick (1999) extinction curve is parametrized as a function of R_V. Therefore, one can obtain the extinction curve computed for the case $R_V = 2.5$ with a seventh-degree polynomial fitting in the form

$$\frac{A_\lambda}{E(B-V)} = \sum_{n=0}^{7} a_n x^n, \qquad (1)$$

with $x = 1/\lambda$ (μm^{-1}). Table 5 shows the coefficients of the polynomial fitting obtained using equation (1).

We determined the reddening from the optical spectra, using the H α and H β Balmer lines and assuming a dereddened H α/H β flux ratio as given by the recombination theory: I(H α)/I(H β) $\sim$ 2.86. Column 3 of Table 6 shows the extinction $E(B-V)$ obtained for each object of our sample. The reddening showed in this table was applied both in the optical and NIR spectra. The remaining columns of Table 6 list the electron densities and temperatures and will be introduced in Section 3.

2.2.4 *Line-flux uncertainties*

Sources of errors in the flux measurements can be photon shot and CCD readout noise, bias and sky background induced noise, and errors in the standard star calibration and in the interstellar and atmospheric extinction corrections. Bad sky-feature subtraction or field star contamination can also contribute to the uncertainties in the line fluxes. The quality of the data can be evaluated since some line ratios are known from atomic physics. For example, the line ratio [O III] $\lambda\lambda$5007/4959 is expected to be 2.98 (Storey & Zeippen 2000). Fig. 6 shows the [O III] $\lambda\lambda$5007/4959 ratio as a function of the [O III] λ5007 line flux. The dashed line shows the theoretical value of

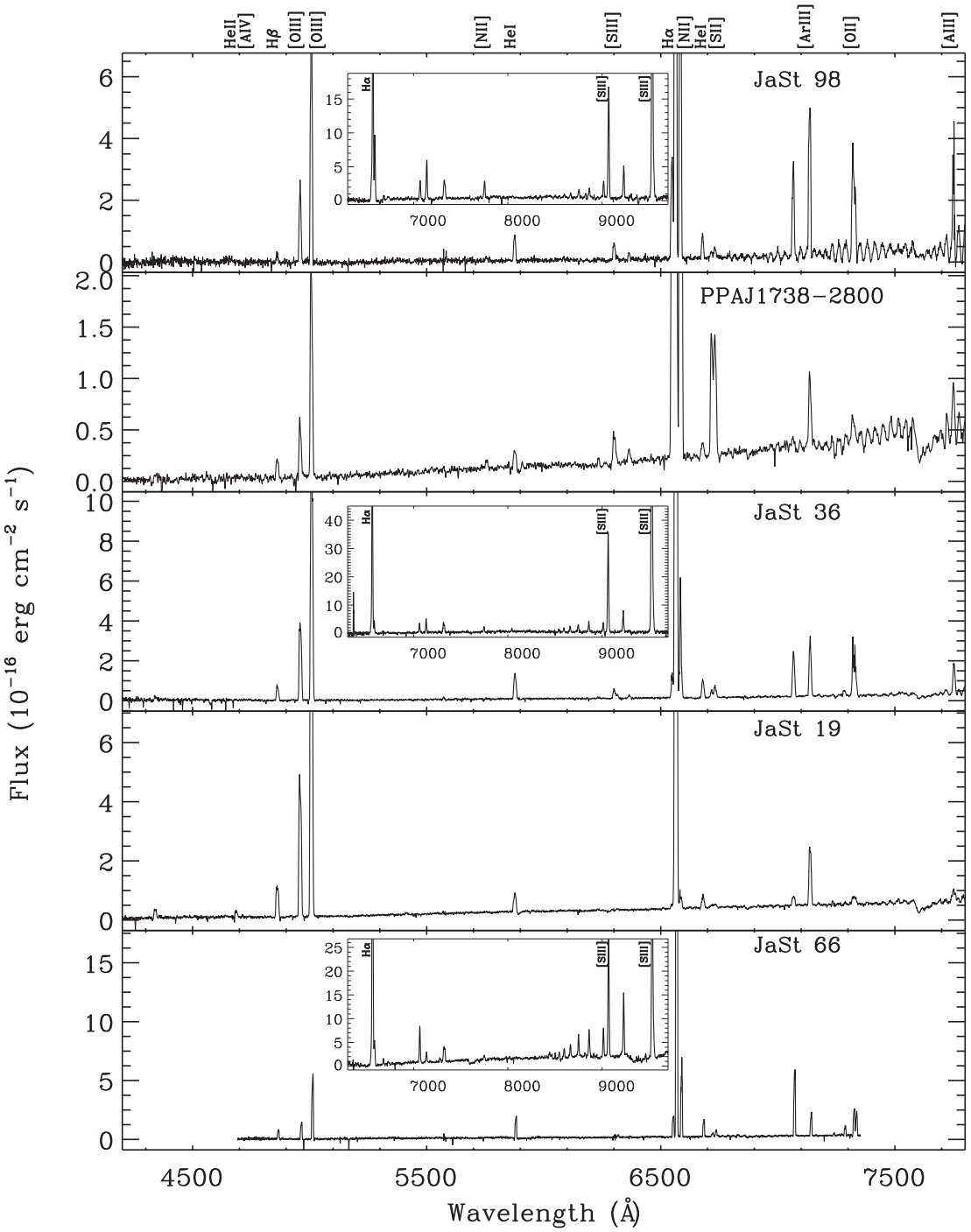

Figure 4. Calibrated optical spectra of low and medium resolution of the GBPNe observed. In the centre top of each optical spectra, the respective NIR spectrum is shown, when available.

2.98, and the shaded area corresponds to expected uncertainty of 5 per cent around this value. The dispersion of the observed ratios in this figure is consistent with an uncertainty of 5 per cent in the flux measures. It is important to note that in cases of lines with a lower S/N or strong blending, the uncertainty is higher and can reach 40 per cent in the worst cases. In cases of strong line blending, as in the 2010 observations due to the low resolution of the 300 l mm^{-1} grating, the flux of the line [N II] λ6548 was calculated from the known ratio [N II] λλ6584/6548 of 3 (Osterbrock & Ferland 2006).

Fig. 7 shows the ratio of [S III] λ9532 and [S III] λ9069 fluxes as a function of the [S III] λ9532 line flux. The theoretical predicted value by atomic physics of 2.44 is shown in the figure for reference. As can be seen in Figs 6 and 7, most of the flux ratios are consistent with a line uncertainty of 5 per cent. In the case of [O III], all but two objects PPA J1738−2800 and JaSt 98 have line ratios compatible with flux uncertainties within 10 per cent. In the case of [S III], objects JaSt 19, JaSt 23, JaSt 46, JaSt 52 and JaSt 77 have line ratios compatible with flux uncertainties of 5 per cent. Objects JaSt 36, JaSt 64 and

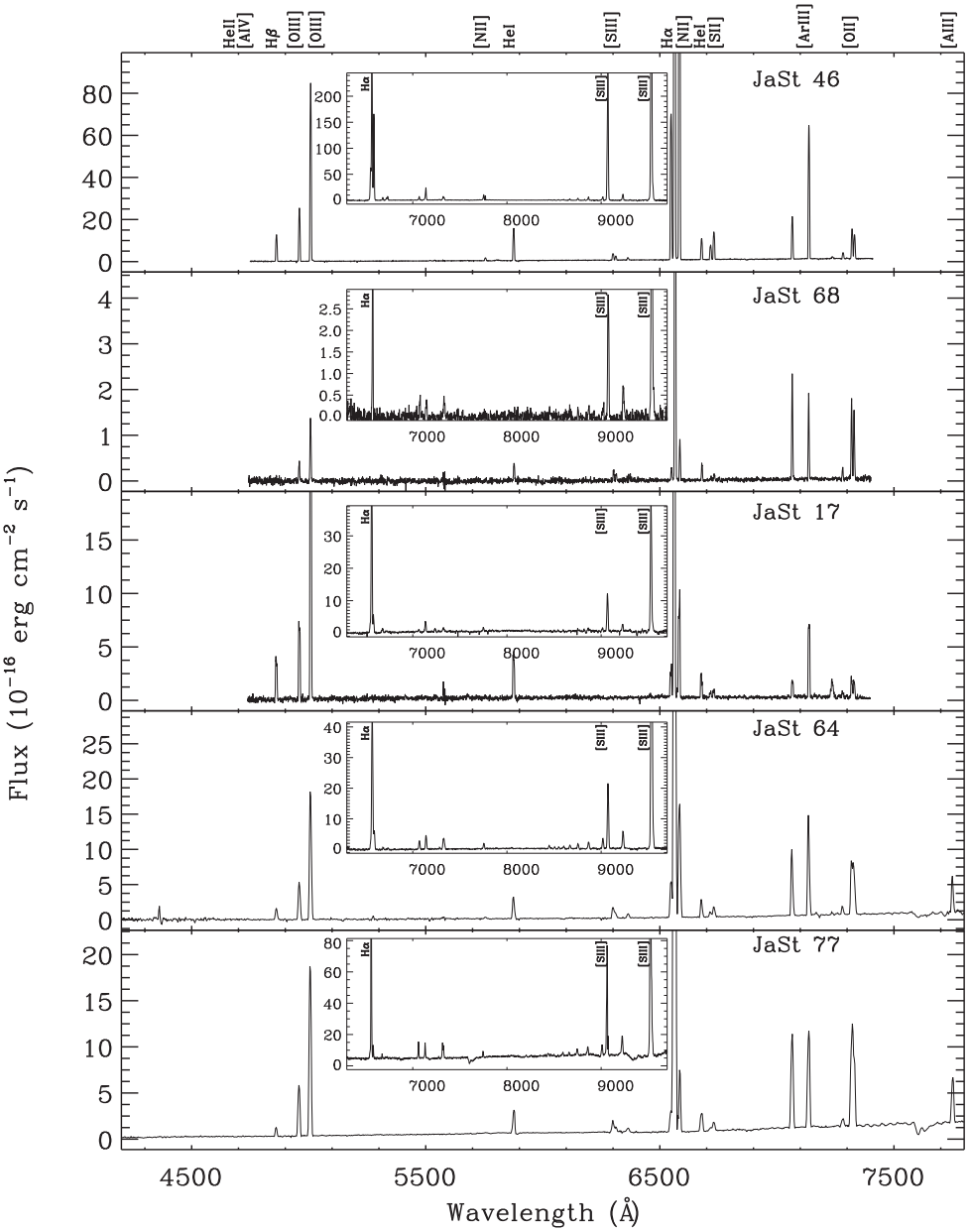

Figure 4 – *continued*

JaSt 66 have flux uncertainties larger than 15 per cent. Probably, a better flux calibration and spectrum extraction and/or correction for telluric lines are needed for these objects. In the case of objects having [S III] line ratios higher than 2.44, a telluric absorption in [S III] λ9069 may be indicated. Those having [S III] line ratios lower than the theoretical value may indicate an absorption in [S III] λ9532. Therefore, some caution should be devoted in the electronic temperature from [S III] lines for these objects. The PN JaSt 79 shows a stellar continuum at the NIR in its spectrum that is not observed in the other PNe of our sample. Indeed, this object was classified as a symbiotic star by Miszalski et al. (2009). Also, our spectrum of this object shows high ionization lines as [Fe VII] λλ5721, 6087, with reddened fluxes 1.154×10^{-15} and 3.240×10^{-15} erg cm^{-2} s^{-1}, respectively, confirming its symbiotic nature. Therefore, this object will be excluded from the abundance analysis performed in Section 4.

3 DETERMINATION OF PHYSICAL PARAMETERS, IONIC AND TOTAL ABUNDANCES

3.1 Physical parameters

Table 6 shows the electron densities derived from [S II] λλ6731/6717 line ratios. In the same table, we list the electron temperatures obtained from [N II] λ5755/(6584+6548) line ratios and [S III] λ6312/(9532+9069).

The [O III] temperatures were derived from a linear correlation with [S III] temperatures obtained by Henry, Kwitter & Balick (2004):

$$T_{e[S\,III]} = -0.039(\pm 0.11) + 1.20(\pm 0.11) \times T_{e[O\,III]}, \quad (2)$$

where temperatures are in units of 10^4 K. Henry et al. (2004) estimated that the [S III] temperatures can be obtained from this

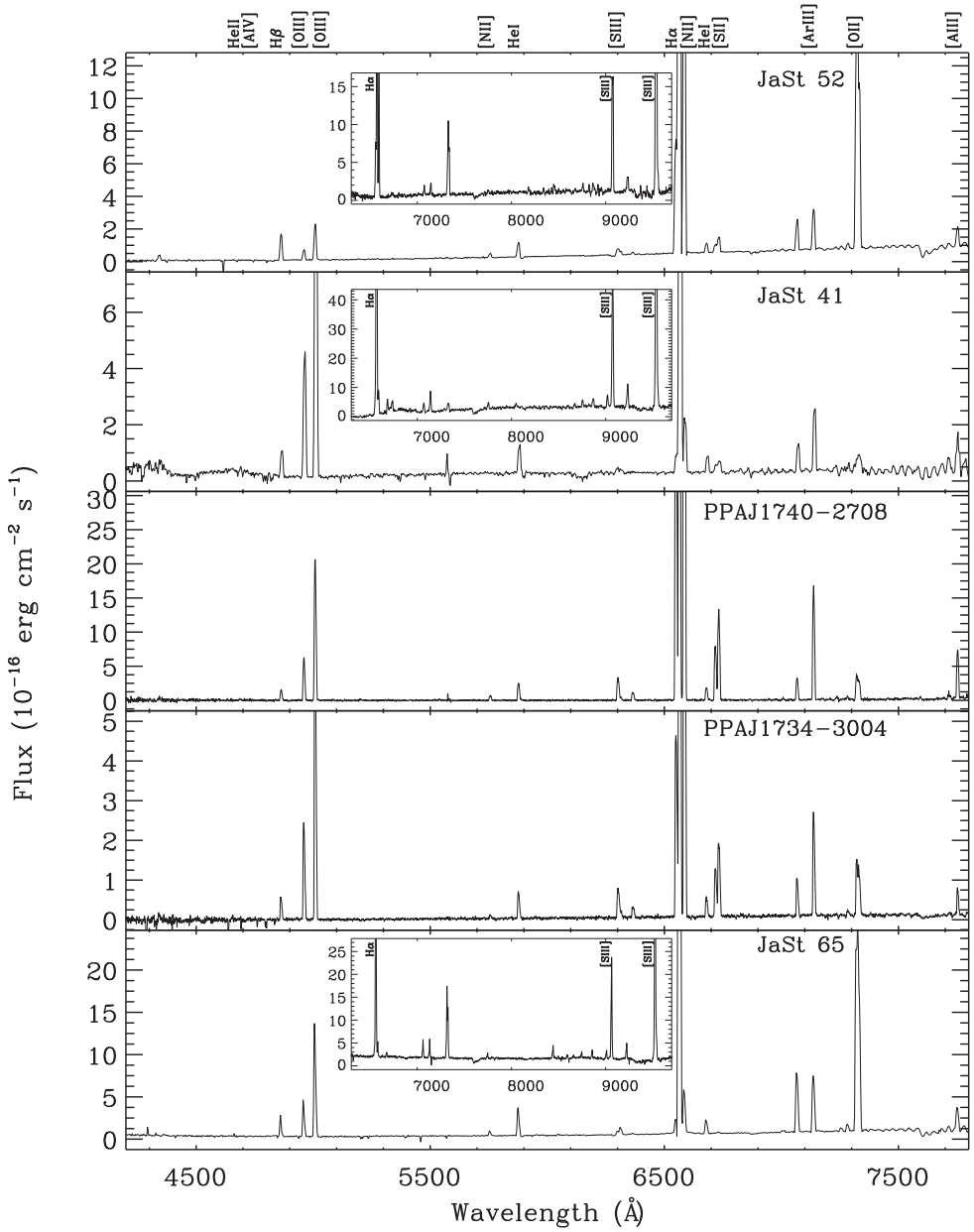

Figure 4 – *continued*

equation with an uncertainty of ∼1000 K. The $T_{e[O\,III]}$ temperatures calculated from this linear correlation included in Table 6 also are listed with errors. The errors were calculated from the Monte Carlo procedure explained in Section 3.4 and only include line-flux uncertainties. We prefer to use $T_{e[O\,III]}$ calculated from the $T_{e[S\,III]}$. However, in some cases $T_{e[S\,III]}$ was very low to calculate $T_{e[O\,III]}$ from equation (2). In these few cases, we adopted $T_{e[N\,II]}$ instead of $T_{e[O\,III]}$ and they are listed without errors in Table 6. We derived T_e from [S III] only in the cases where the line ratio 9532/9069 was within the dashed lines of Fig. 7. By doing this, the individual line fluxes should have errors 10 per cent or lower.

As discussed in Section 2, objects JaSt 36, JaSt41 and JaSt 64 have uncertainties in the [S III] 9532 and 9069 Å lines fluxes higher than 15 per cent. This can introduce higher errors in the electron temperatures obtained from [S III]. In the case of JaSt 64, we opted to use $T_{e[O\,III]}$ from $T_{e[N\,II]}$. In the cases of JaSt 41 and JaSt 66 where the observed ratio was lower than the theoretical one, indicating a stronger absorption in the 9532 line, the total dereddened [S III] intensity was taken equal to 2.44 times the 9069 line. In the remaining cases (JaSt 17, JaSt 36 and JaSt 98) where the ratio was larger than the theoretical one, the 9532 line was taken as reference instead. Examining in detail the spectra of JaSt 41, we noted a contamination by a field star. Therefore, some caution should be taken with the results for this object.

In the case of object JaSt 65, we obtained a non-physical value of 27 083 K for the temperature from [S III] lines. This temperature is not typical for PNe, and to calculate the abundances for this object we adopted an upper limit of 2×10^4 K for $T_{e[O\,III]}$ and $T_{e[N\,II]}$. However, since the abundances derived from collisional excitation lines strongly depend on the temperatures, the uncertainties in the abundances for this object are very high. Therefore, this object will not be used in the abundance analysis. JaSt 79 was also excluded

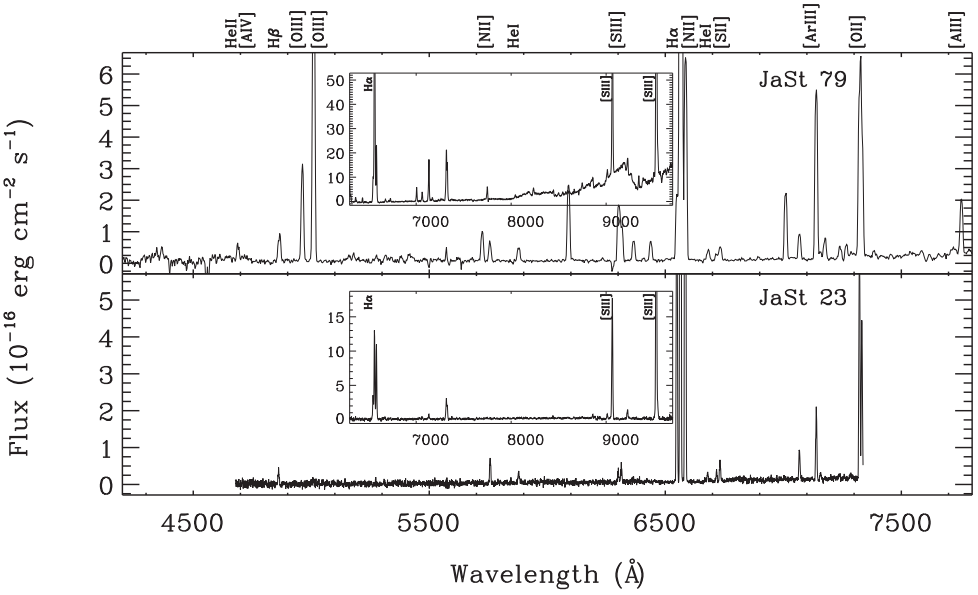

Figure 4 – *continued*

Table 4. Reddened fluxes relative to H β. F(H β) is in units of erg cm^{-2} s^{-1}. The entire content is available electronically.

		0.344+1.567[a] JaSt 23		000.2+01.7 JaSt 19		000.2−01.4 JaSt 79		000.4+01.1 JaSt 36	
λ	Ion	$F(\lambda)/F(\mathrm{H}\,\beta)$	Error	$F(\lambda)/F(\mathrm{H}\,\beta)$	Error	$F(\lambda)/F(\mathrm{H}\,\beta)$	Error	$F(\lambda)/F(\mathrm{H}\,\beta)$	Error
4341	H γ	–	–	0.24	0.02	0.32	0.03	0.17	0.02
4363	O III	–	–	0.04	0.01	0.39	0.04	–	–
4686	He II	–	–	0.15	0.02	0.46	0.05	–	–
4861	H β+He II	1.00	0.10	1.00	0.10	1.00	0.10	1.00	0.10
4959	O III	–	–	3.95	0.40	3.17	0.32	5.65	0.28
5007	O III	0.22	0.02	13.29	0.66	10.82	0.54	17.70	0.89
5412	He II	–	–	0.06	0.01	0.38	0.04	–	–
5518	Cl3	–	–	–	–	–	–	–	–
5538	Cl3	–	–	–	–	–	–	–	–
5755	N II	1.66	0.17	0.02	0.01	0.60	0.06	0.03	0.01
5876	He I	0.85	0.09	0.52	0.05	0.51	0.05	1.76	0.18
6300	O I	0.79	0.08	–	–	2.06	0.21	0.54	0.05
6312	S III	1.09	0.11	0.03	0.01	1.11	0.11	0.29	0.03
6363	O I	–	–	–	–	0.71	0.07	0.19	0.02
6435	Ar V	–	–	–	–	0.66	0.07	–	–
6548	N II	19.18	0.96	0.11	0.01	2.21	0.22	1.56	0.16
6563	H α	73.86	3.69	30.06	1.50	36.68	1.83	74.44	3.72
6584	N II	56.23	2.81	0.35	0.03	6.64	0.33	4.91	0.49
6678	He I	0.85	0.09	0.38	0.04	0.44	0.04	1.26	0.13
6716	S II	0.76	0.08	0.10	0.02	0.23	0.02	0.47	0.05
6731	S II	1.42	0.14	0.12	0.01	0.51	0.05	0.77	0.08
7005	Ar V	–	–	–	–	2.37	0.24	–	–
7065	He I	2.19	0.22	0.30	0.03	0.89	0.09	2.91	0.29
7135	Ar III	4.66	0.47	1.66	0.17	6.05	0.30	3.59	0.36
7237	Ar IV	–	–	0.07	0.01	0.44	0.04	–	–
7263	Ar IV	–	–	–	–	0.50	0.05	–	–
7281	He I	–	–	–	–	–	–	0.41	0.04
7322	O II	14.79	0.74	0.37	0.04	9.76	0.49	2.28	0.23
7333	O II	10.26	0.51	–	–	–	–	1.98	0.20
7751	Ar III	–	–	0.44	0.04	1.98	0.20	1.91	0.19
9069	S III	115.23	5.76	–	–	21.11	1.06	49.06	2.45
9532	S III	355.35	17.77	–	–	52.47	2.62	151.65	7.58
log (FH β)		−15.602		−14.856		−14.919		−15.079	

[a]OH 0.3447+1.5656.

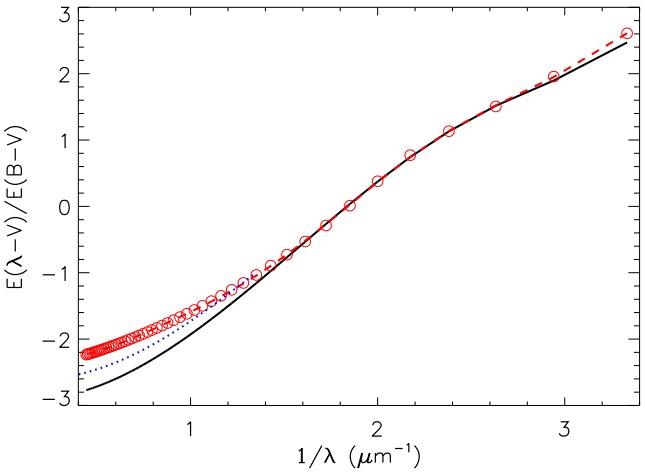

Figure 5. Normalized interstellar extinction curves from NIR through optical. Open circles are the data generated using the Fitzpatrick (1999) extinction parametrization in the case $R \equiv A(V)/E(B-V) = 2.5$. The dashed line represents the seventh-degree polynomial fit. The black continuous line shows the same parametrization for the case $R_V = 3.1$. The dotted line corresponds to the NIR extinction parametrization from Fitzpatrick & Massa (2009) in the case of $R_V = 2.64$ and $\alpha = 2.49$.

Table 5. Coefficients of the parametrized extinction curve.

n	0	1	2	3	4	5	6	7
a_n	1.29	−7.80	20.60	−24.84	16.77	−6.21	1.17	−0.09

from the abundance analysis because of its symbiotic nature. This can be noted in Table 6, where the derived [S III] electron temperature yielded 43 105 K, a very high value for a typical PNe. The electronic temperature from [N II] for JaSt 23 is also non-typical for PNe. None the less, $T_{e[S\,III]}$ resulted in a plausible value. In view of the discrepancy between both values, some caution should be taken with the chemical abundances of this object and we prefer not to use its abundances in the abundance analysis.

3.2 Ionic abundances

The abundance for He^+ was derived from the average of the recombination lines 4471, 5876 and 6678 Å. The average was weighted by the intensity of each line. New He I emissivities have recently become available through the work of Porter et al. (2012) and recently corrected by Porter et al. (2013). These are the most recent He I emissivities, and collisional effects are already included in the emissivities calculation. In this work, the emissivities of Porter et al. (2013) are adopted in order to calculate the He I abundances. Their emissivities are tabulated for discrete electron densities and temperatures. Therefore, we fitted the values provided by Porter et al. (2013) for $n_e = 10^3$ and 10^4 cm^{-3} and T_e between 5×10^3 and 2.5×10^4 K using the following parametrization:

$$\frac{4\pi j_\lambda}{n_e n_{He^+}} = \left[a + b(\ln T_e)^2 + c \ln T_e + \frac{d}{\ln T_e}\right] T_e^{-1}, \quad (3)$$

in units of 10^{-25} erg cm^3 s^{-1}. The results are shown in Fig. 8, where the He I emissivities for the lines 4471, 5876 and 6678 Å are displayed as a function of the electron temperature, for two values of electron densities: 10^3 cm^{-3} (red circles) and 10^4 cm^{-3} (black squares). Fits using equation (3) are displayed in the same figure as dotted lines ($n_e = 10^3$ cm^{-3}) and continuous lines ($n_e = 10^4$ cm^{-3}). The coefficients of the fits using equation (3) are shown in Table 7.

Values between the fitted functions displayed in Fig. 8 were interpolated on a logarithmic scale following Monreal-Ibero et al. (2013) as

$$j^*_\lambda[\log(n_e)] = [j^*_\lambda(4) - j^*_\lambda(3)] \times [\log(n_e) - 3] + j^*_\lambda(3), \quad (4)$$

where we defined $j^*_\lambda = 4\pi j_\lambda / n_e n_{ion}$, with $n_{ion} = n_{He^+}$ in this particular case.

In our code, the He^{+2} abundance is calculated from the He II 4686 Å recombination line. The recombination coefficients

Table 6. Extinction and physical parameters.

PNG	Name	$E(B-V)$	n_e [S II] (cm^{-3})	T_e [N II] (K)	T_e [O III] (K)	T_e [S III] (K)
0.344+1.567[a]	JaSt 23	2.94 ± 0.12	7159	41 566[b]	11 260	13 122 ± 1103
000.2+01.7	JaSt 19	2.13 ± 0.12	1110	11 442 ± 1095	11 442[c]	–
000.2 − 01.4	JaSt 79	2.31 ± 0.12	19 064 ± 1299	20 000[d]	20 000[d]	43 105[b]
000.4+01.1	JaSt 36	2.95 ± 0.15	3597	11 018 ± 1552	11 018[c]	10 296
000.5+01.9	JaSt 17	1.95 ± 0.13	2077 ± 1077	12 836 ± 1934	12 836[c]	7414 ± 600
000.6 − 01.0	JaSt 77	3.46 ± 0.13	16 006	11 454[e]	11 454	13 355 ± 1992
000.9+01.8	PPA J1740−2708	2.56 ± 0.11	3892 ± 1111	9867 ± 533	9867[c]	–
001.0+01.3	JaSt 41	3.07 ± 0.11	2336 ± 1929	10 712[e]	10 712	12 464 ± 840
001.5+01.5	JaSt 46	2.26 ± 0.11	7235	9653 ± 1226	9653[c]	7110 ± 335
001.7+01.3	JaSt 52	2.44 ± 0.12	11 470	13 308 ± 2154	13 308[c]	6948 ± 592
002.0 − 01.3	JaSt 98	3.42 ± 0.13	3035	14 135 ± 1357	10 258 ± 1357	11 920
357.7+01.4	PPA J1734−3004	2.57 ± 0.12	3529 ± 2255	11 665 ± 970	11 665[c]	–
358.5 − 01.7	JaSt 64	3.06 ± 0.13	12 520	15 533 ± 2785	15 533[c]	11 755 ± 1209
358.9 − 01.5	JaSt 65	2.98 ± 0.13	6689	20 000[d]	20 000[d]	27 083[b]
359.5 − 01.2	JaSt 66	3.26 ± 0.12	2678 ± 1600	11 184[e]	11 184	13 030 ± 1361
359.5 − 01.3	JaSt 68	3.81 ± 0.12	6701 ± –	13 441[e]	13 441	15 739 ± 2083
359.9+01.8	PPA J1738−2800	1.86 ± 0.13	2420 ± 875	12 749 ± 1001	12 749[c]	–

[a] OH 0.344 +1.567.
[b] Non-physical value.
[c] Adopted from T_e [N II].
[d] Upper limit adopted.
[e] Adopted from T_e [O III].

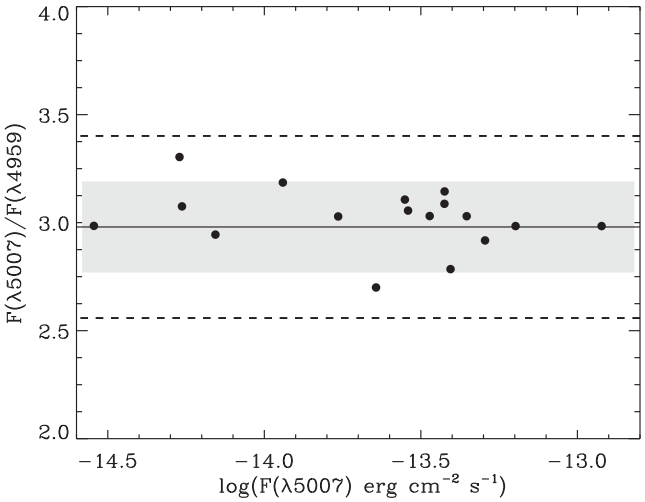

Figure 6. Ratio of [O III] λ5007 and [O III] λ4959 fluxes as a function of the [O III]λ5007 line flux. The horizontal dashed line shows the theoretical flux ratio [O III] λλ5007/4959 of 2.98. The shaded area corresponds to the expected uncertainty in the line ratios, considering an error of 5 per cent in the line fluxes. The dashed lines corresponds to the expected uncertainty in the line ratios, considering an error of 10 per cent in the line fluxes.

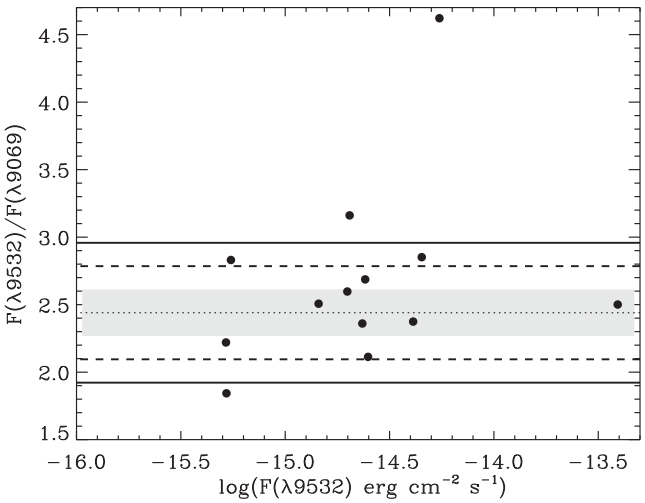

Figure 7. Ratio of [S III] λ9532 and [S III] λ9069 fluxes as a function of the [S III] λ9532 line flux. The horizontal dotted line shows the theoretical flux ratio of 2.44. The shaded area corresponds to the expected uncertainty in the line ratios, considering an error of 5 per cent in the line fluxes. The dashed and solid lines correspond to the expected uncertainty in the line ratios, considering an error of 10 and 15 per cent in the line fluxes, respectively.

tabulated in Osterbrock & Ferland (2006) were used as well as the H β emissivity provided by Aver, Olive & Skillman (2010). We fitted the ratio $j^*_{\lambda4861}/j^*_{\lambda4686}$ with a second-degree polynomial function. For typical densities found in PNe, this ratio does not depend strongly on the density, so we adopted $n_e = 10^4 \mathrm{cm}^{-3}$ and the result of the fit is shown in equation (5). Both He^+ and He^{+2} abundances are calculated using the O III electron temperature,

$$\frac{j^*_{\lambda4861}}{j^*_{\lambda4686}} = 5.1340 - 5.062 \times 10^{-4}\, T_e + 1.4280 \times 10^{-8}\, T_e^2. \quad (5)$$

For collisionally excited lines, we calculated the ionic abundances using the NEBULAR software (Shaw & Dufour 1995) and the appropriate electron temperature for the corresponding ionization zone.

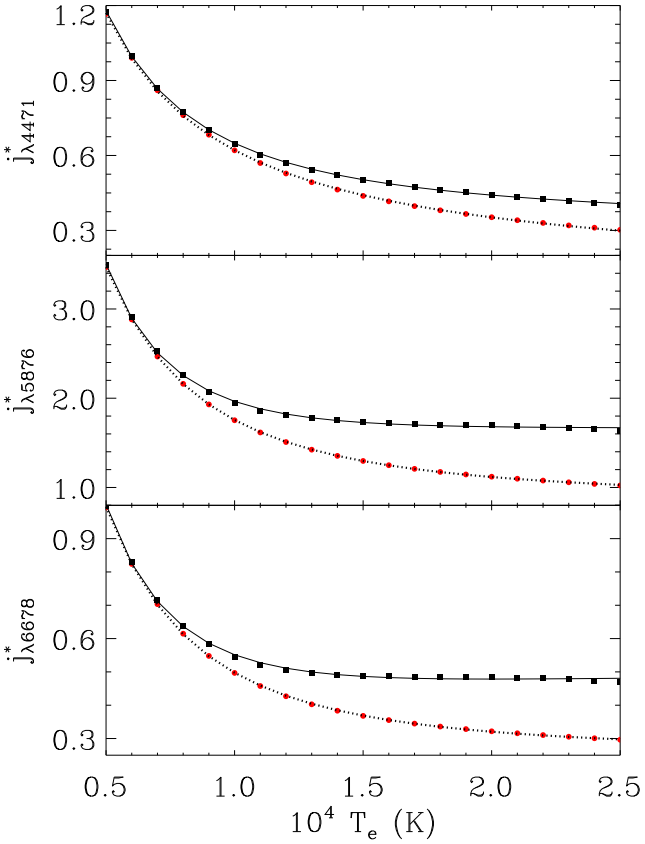

Figure 8. Emissivities of He I from Porter et al. (2013) as a function of the electron temperature T_e for two different values of electron density and fitted functions: 10^3 cm^{-3} (red circles, dotted lines) and 10^4 cm^{-3} (black squares, continuous lines). The emissivities are expressed as $j^*_\lambda = 4\pi j_\lambda / n_e n_{He^+}$ in units of 10^{-25} erg cm^3 s^{-1}.

Table 7. Coefficients for the He I emissivities.

λ (Å)	$a \times 10^6$	$b \times 10^3$	$c \times 10^5$	$d \times 10^6$
		$n_e = 10^3$ cm^{-3}		
4471	0.522 35	−2.394 94	−0.607 26	−1.473 58
5876	7.136 71	31.326 93	−8.181 63	−20.641 05
6678	2.170 62	9.556 00	−2.492 80	−6.266 13
		$n_e = 10^4$ cm^{-3}		
4471	2.007 19	9.161 67	−2.343 19	−5.707 99
5876	9.737 06	46.876 04	−11.702 38	−26.853 40
6678	3.310 42	15.594 03	−3.935 18	−9.240 89

3.3 Elemental abundances

Since the spectral range of the observations is not sufficient to observe all the necessary lines of a given ion, it is not possible to calculate the total abundance of a particular element by the direct sum of the ionic abundances of all the ions present in a nebula. Instead, it must be calculated by means of the ionization correction factors (ICFs). One of the most frequently used ICFs in the literature are those from Kingsburgh & Barlow (1994). However, recently Delgado-Inglada, Morisset & Stasińska (2014) have published new ICF formulae based on a grid of photoionization models and they have computed analytical expressions for the ICFs of He, O, N, Ne, S, Ar, Cl and C. According to their work, the oxygen abundances are not expected to be very different from those

Table 8. Ionic abundances.

PNG	He^+	He^{++}	O^+ $\times 10^{-4}$	O^{++} $\times 10^{-6}$	N^+ $\times 10^{-6}$	S^+ $\times 10^{-6}$	S^{++} $\times 10^{-6}$	Ar^{++} $\times 10^{-6}$
0.344+1.567[a]	0.058 ± 0.007	–	0.66	0.06	33.57	0.27	7.30	0.66
000.2+01.7	0.075 ± 0.010	0.018 ± 0.003	0.08	2.28	0.44 ± 0.15	0.04 ± 0.01	0.55	0.64
000.2 − 01.4	0.034 ± 0.004	0.059 ± 0.011	0.08 ± 0.01	0.45 ± 0.05	2.75 ± 0.30	0.13 ± 0.02	1.74	0.70 ± 0.06
000.4+01.1	0.117 ± 0.016	–	0.14	3.11 ± 1.39	2.90 ± 1.18	0.11 ± 0.06	2.35 ± 1.50	0.57 ± 0.21
000.5+01.9	0.143 ± 0.018	–	0.05	0.79 ± 0.39	3.09 ± 1.23	0.06 ± 0.02	0.53	0.73 ± 0.23
000.6 − 01.0	0.121 ± 0.013	–	0.33	2.94	2.01	0.17	2.36	0.84
000.9+01.8	0.165 ± 0.017	0.019 ± 0.003	0.94 ± 0.34	3.60 ± 0.78	126.05 ± 23.66	2.88 ± 0.76	7.75 ± 2.39	3.56 ± 0.65
001.0+01.3	0.131 ± 0.016	–	0.32	1.25	3.45	0.06	2.03	0.32
001.5+01.5	0.134 ± 0.017	–	0.29 ± 0.24	1.85 ± 0.89	31.55 ± 14.32	0.61	3.91	2.23 ± 0.70
001.7+01.3	0.049 ± 0.006	–	0.53 ± 0.37	0.14 ± 0.06	9.93 ± 5.30	0.21	0.50	0.34 ± 0.11
002.0 − 01.3	0.130 ± 0.018	–	0.17 ± 0.07	2.15 ± 0.52	7.17 ± 1.77	0.06 ± 0.03	0.93	0.97 ± 0.21
357.7+01.4	0.113 ± 0.015	–	0.21 ± 0.09	2.19 ± 0.59	22.76 ± 5.77	0.79	6.14 ± 1.95	0.96 ± 0.23
358.5 − 01.7	0.083	–	0.06	0.76	3.16	0.12	1.31	0.51
358.9 − 01.5	0.076 ± 0.011	–	0.10	0.26	0.67	0.01	0.71	0.22
359.5 − 01.2	0.120 ± 0.013	–	0.11	1.03	2.97	0.06	1.32	0.22
359.5 − 01.3	0.115	–	0.08	1.15	1.18	0.05	2.20	0.46
359.9+01.8	0.123 ± 0.013	–	0.25 ± 0.09	1.04 ± 0.22	47.11 ± 10.15	2.14 ± 0.49	2.52 ± 0.79	1.79 ± 0.40

[a]OH 0.3447+1.5656.

calculated with the ICFs of Kingsburgh & Barlow (1994). On the other hand, the abundances of N, S, Ar, Ne calculated with the new ICFs show significant differences. A direct comparison between the abundances calculated with both ICFs is beyond the scope of this paper and the reader is referred to the original paper of Delgado-Inglada et al. (2014), where some comparisons are done between both ICFs. However, one should mention that a direct comparison between the abundances of N, S, Ar and Ne calculated with both ICFs is missing in that paper.

In our code PNPACK, we have implemented the calculation of the elemental abundances by using the ICFs provided by Delgado-Inglada et al. (2014) and also Kingsburgh & Barlow (1994). In this paper, we are adopting the new ICFs proposed by Delgado-Inglada et al. (2014) since they incorporate more recent physics and are derived using a wider range of parameters of photoionization models than the previous ICFs from Kingsburgh & Barlow (1994). One advantage of the new ICFs provided by Delgado-Inglada et al. (2014) is the possibility to compute the errors in the elemental abundances introduced by the adopted ICF approximation. They provide analytical formulae to estimate error bars associated with the ICFs, something not possible until their work. In the case of helium, we opted not to use any ICF since the relative populations of helium essentially ions depend on the effective temperature of the central star. Therefore, there is no reliable way to correct for neutral helium in our objects.

The reader should note that in some cases, where the ionic abundance was available, the elemental abundance of the corresponding ion was not possible to calculate since the ICFs of Delgado-Inglada et al. (2014) are not valid for the specific v and w parameters (see Delgado-Inglada et al. 2014, for more details). In these few cases, in order to obtain the elemental abundances one needs to perform detailed photoionization models of the object. The obtained ionic abundances relative to hydrogen and uncertainties are shown in Table 8.

In order to test the ICFs, Fig. 9 shows the values of $(He^+ + He^{++})/H$, S/O and Ar/O as a function of $O^{++}/(O^+ + O^{++})$. No significant trend is seen for S/O and Ar/O. For $(He^+ + He^{++})/H$, since for many PNe we have not detected the presence of He^{++} lines, the helium abundances are a lower limit for these objects. For low excitation objects the uncertainties in the helium abundances are very high, as shown by the error bars in the figure. This can be attributed to neutral helium as it is not taken into account by the helium ICF.

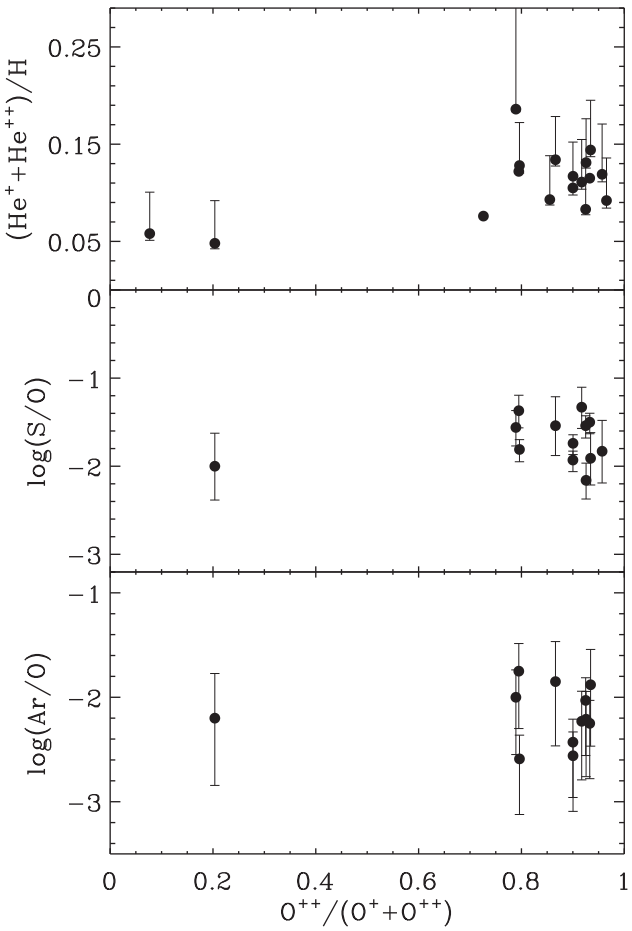

Figure 9. Abundance ratios of $(He^+ + He^{++})/H$, S/O and Ar/O as a function of $O^{++}/(O^+ + O^{++})$ in top, middle and bottom panels, respectively.

Table 9. Elemental abundances.

PNG	Name	He/H	12+log O/H	12+log N/H	12+log S/H	12+log Ar/H
0.344 + 1.567[a]	JaSt 23	$0.058^{+0.326}_{-0.003}$	$7.85^{+0.16}_{-0.16}$	$7.61^{+0.17}_{-0.17}$	$6.87^{+0.18}_{-0.20}$	$6.11^{+0.26}_{-0.55}$
000.2 + 01.7	JaSt 19	$0.092^{+0.042}_{-0.005}$	$8.43^{+0.13}_{-0.13}$	–	$6.13^{+0.17}_{-0.19}$	–
000.2 − 01.4	JaSt 79	$0.093^{+0.047}_{-0.006}$	$8.04^{+0.12}_{-0.15}$	$7.49^{+0.22}_{-0.22}$	$6.71^{+0.15}_{-0.19}$	$6.29^{+0.25}_{-0.55}$
000.4 + 01.1	JaSt 36	$0.119^{+0.043}_{-0.007}$	$8.52^{+0.20}_{-0.20}$	$8.44^{+0.31}_{-0.30}$	$6.69^{+0.29}_{-0.30}$	–
000.5 + 01.9	JaSt 17	$0.144^{+0.044}_{-0.008}$	$7.92^{+0.19}_{-0.19}$	$8.27^{+0.28}_{-0.27}$	$6.01^{+0.22}_{-0.24}$	$6.04^{+0.28}_{-0.56}$
000.6 − 01.0	JaSt 77	$0.105^{+0.045}_{-0.006}$	$8.51^{+0.05}_{-0.05}$	$7.88^{+0.24}_{-0.23}$	$6.58^{+0.09}_{-0.12}$	$6.08^{+0.21}_{-0.53}$
000.9 + 01.8	PPA J1740−2708	$0.186^{+0.052}_{-0.008}$	$8.68^{+0.11}_{-0.11}$	$8.80^{+0.20}_{-0.19}$	$7.12^{+0.16}_{-0.18}$	$6.68^{+0.24}_{-0.54}$
001.0 + 01.3	JaSt 41	$0.128^{+0.051}_{-0.007}$	$8.20^{+0.06}_{-0.06}$	$7.74^{+0.20}_{-0.19}$	$6.39^{+0.09}_{-0.13}$	$5.61^{+0.22}_{-0.53}$
001.5 + 01.5	JaSt 46	$0.134^{+0.047}_{-0.007}$	$8.33^{+0.21}_{-0.21}$	$8.94^{+0.32}_{-0.31}$	$6.79^{+0.25}_{-0.27}$	$6.48^{+0.32}_{-0.58}$
001.7 + 01.3	JaSt 52	$0.048^{+0.173}_{-0.003}$	$7.85^{+0.24}_{-0.24}$	$7.26^{+0.31}_{-0.31}$	$5.85^{+0.29}_{-0.30}$	$5.65^{+0.35}_{-0.60}$
002.0 − 01.3	JaSt 98	$0.131^{+0.044}_{-0.008}$	$8.38^{+0.12}_{-0.12}$	$8.59^{+0.26}_{-0.25}$	$6.22^{+0.15}_{-0.17}$	$6.17^{+0.24}_{-0.54}$
357.7 + 01.4	PPA J1734−3004	$0.111^{+0.044}_{-0.006}$	$8.38^{+0.12}_{-0.12}$	$9.02^{+0.25}_{-0.24}$	$7.05^{+0.19}_{-0.21}$	$6.15^{+0.26}_{-0.55}$
358.5 − 01.7	JaSt 64	$0.083^{+0.044}_{-0.006}$	$7.92^{+0.05}_{-0.05}$	$8.22^{+0.22}_{-0.21}$	$6.38^{+0.10}_{-0.13}$	$5.89^{+0.21}_{-0.53}$
358.9 − 01.5	JaSt 65	$0.076^{+0.056}_{-0.005}$	$7.56^{+0.01}_{-0.01}$	$6.85^{+0.17}_{-0.15}$	$5.88^{+0.05}_{-0.10}$	$5.40^{+0.33}_{-0.58}$
359.5 − 01.2	JaSt 66	$0.117^{+0.045}_{-0.006}$	$8.06^{+0.05}_{-0.05}$	$8.05^{+0.23}_{-0.22}$	$6.32^{+0.08}_{-0.12}$	$5.50^{+0.22}_{-0.53}$
359.5 − 01.3	JaSt 68	$0.115^{+0.044}_{-0.007}$	$8.09^{+0.05}_{-0.05}$	$7.84^{+0.27}_{-0.26}$	$6.59^{+0.09}_{-0.12}$	$5.84^{+0.21}_{-0.53}$
359.9 + 01.8	PPA J1738−2800	$0.122^{+0.051}_{-0.006}$	$8.10^{+0.10}_{-0.10}$	$8.86^{+0.21}_{-0.20}$	$6.73^{+0.14}_{-0.17}$	$6.35^{+0.24}_{-0.54}$

[a]OH 0.3447+1.5656.

The obtained chemical abundances and uncertainties (see the next section) of He, O, N, S and Ar with respect to H are listed in Table 9.

3.4 Uncertainties

Uncertainties in the abundances are due to uncertainties in the line fluxes of the abundance diagnostic lines, uncertainties in the diagnostic lines for electron temperature and density, and uncertainties in the ICF that we have assumed for the determination of elemental abundances.

We have computed errors in the abundances and physical parameters, as well as extinction, performing a Monte Carlo procedure. We assumed for each line flux a Gaussian distribution centred at the flux effectively measured and having a dispersion equal to the estimated flux uncertainty. The latter was calculated by comparing the line intensity with that from the H β line. By inspection of our spectra and Figs 6 and 7, we have adopted errors of 5 per cent for lines where the relative flux of the line with H β ($F(\lambda)/F(\mathrm{H}\,\beta)$) was higher than 500. Errors of 10 per cent for those ratios were higher than 10 and lower than 500. An uncertainty of 20 per cent was attributed for ratios $F(\lambda)/F(\mathrm{H}\,\beta)$ higher than 2 and lower than 10. And, finally, errors of 40 per cent was attributed for lines where $F(\lambda)/F(\mathrm{H}\,\beta)$ was lower than 2.

For each line, we considered 250 independent realizations and fitted the histogram of the distribution with a Gaussian function. The error bars and the most probable values were estimated from the Gaussian standard error and mean, respectively, obtained from the Gaussian fit. In the cases where the distribution was clearly not Gaussian, as in most cases of electron densities, we were not able to obtain the errors. These cases are marked with a '–' sign in Tables 6, 8 and 9. An example of a Gaussian fit to the histogram of the Monte Carlo simulation for PN JaSt 36 can be seen in Fig. 10.

The errors in the ICFs were computed through the recent work from Delgado-Inglada et al. (2014), where the authors have evaluated the uncertainties in the ICFs. Thanks to their work, it is now possible to include these uncertainties in the elemental abundances computed with these ICFs. The final uncertainties on the elemental abundances were calculated by adding in quadrature the uncertainties obtained from the ICFs to the uncertainties obtained from the Monte Carlo simulations. Note that, since the uncertainties in the ICFs are not symmetrical, error bars are also not symmetrical for the final abundances.

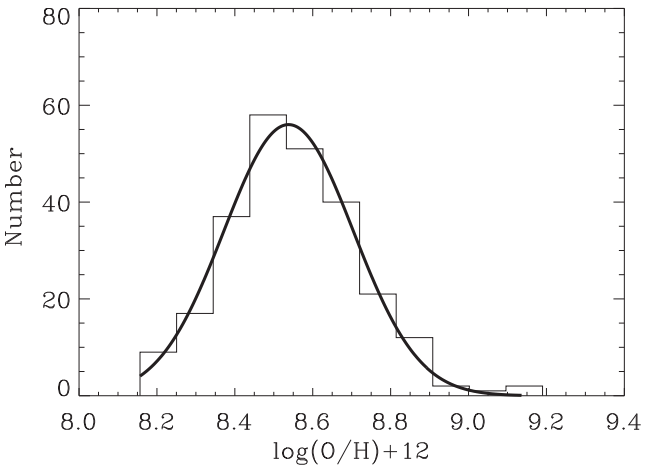

Figure 10. Histogram of log (O/H) + 12 values of the 250 independent realizations from the Monte Carlo simulation for JaSt 36. The continuous curve is the Gaussian fitted to the histogram data.

4 ABUNDANCE ANALYSIS

In order to find differences in the chemical enrichment of GBPNe near the GC and other regions of the Galactic bulge, we compared the abundances obtained in this work with the GBPN abundances from our previous work (CCM10), where we performed spectrophotometric observations of GBPNe located in the outer regions of the bulge. Hence, a comparison between both samples can give information about the chemical enrichment of the central parts of the Milky Way galaxy. We should note that the elemental abundances from CCM10 were calculated with the ICFs from Kingsburgh &

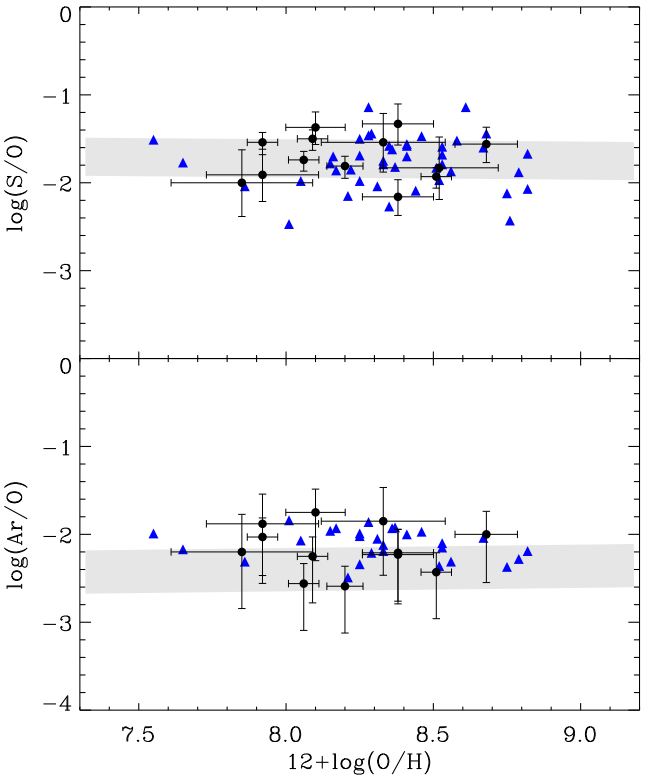

Figure 11. Abundances ratios of S/O and Ar/O as a function of O/H abundances. Black filled circles with error bars are GBPN data from this work. The GBPN data from CCM10 are represented by blue filled triangles. The light-grey bands for α-elements to oxygen ratio represent the 1σ dispersion of the relations from Izotov et al. (2006) for low-metallicity blue compact dwarf galaxies.

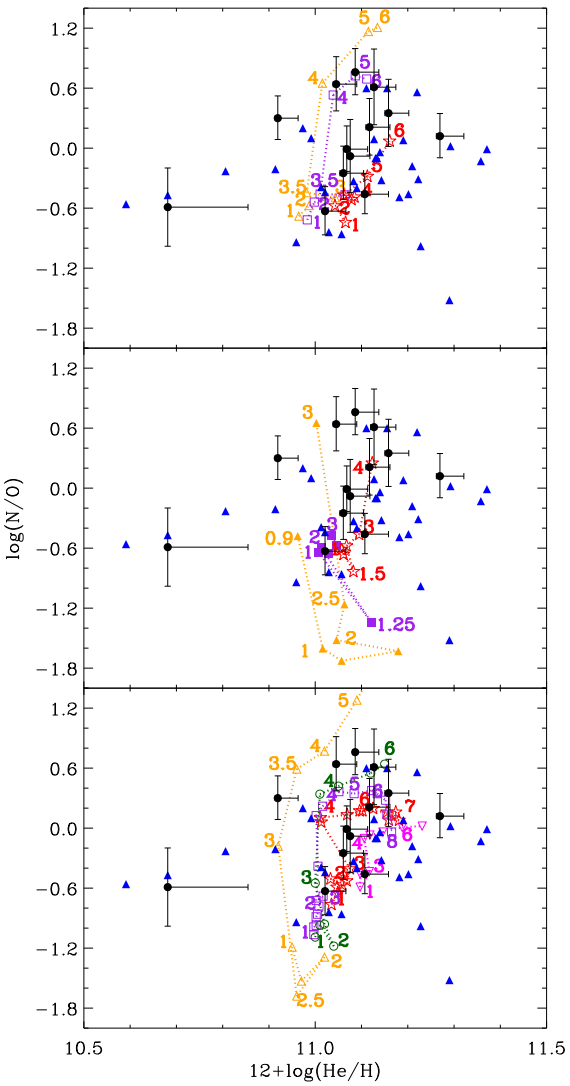

Figure 12. Abundance ratio of N/O as a function of 12 + log(He/H) abundances. Filled circles with error bars are data from this work, while filled blue triangles are the data from CCM10. The open symbols with numbers joined by dotted lines represent the results of the AGB nucleosynthesis models and the numbers give the initial masses of the individual models in $M_{\odot}$ units. Top: models from Karakas (2010) for a given value of Z as orange triangles for $Z = 0.004$, purple squares for $Z = 0.008$ and red stars for $Z = 0.02$; middle: models from Miller Bertolami (2016) as orange triangles for $Z = 0.001$, purple squares for $Z = 0.01$ and red circles for $Z = 0.02$; bottom: models from Ventura et al. group as orange triangles for $Z = 0.001$, green circles for $Z = 0.004$, purple squares for $Z = 0.008$, red stars for $Z = 0.018$ and magenta upside down triangles for $Z = 0.04$.

Barlow (1994) and ours with Delgado-Inglada et al. (2014). To provide a meaningful comparison, we recalculated the abundances from CCM10 with the new ICFs from Delgado-Inglada et al. (2014) and also the He I emissivities from Porter et al. (2013). In this way, we guarantee the same methodology for both samples.

Fig. 11 shows the abundance ratios of S/O and Ar/O as a function of O/H abundances for our data and our previous work (CCM10). The 1σ dispersion of the relations from Izotov et al. (2006) for low-metallicity blue compact dwarf galaxies is displayed in the same figure. The GBPN data seem to follow the Izotov et al. (2006) relations, with most of them inside the 1σ dispersion. We note that our data for the Ar/O ratio show a higher dispersion than the S/O ratio. Our Ar abundances are calculated in most cases from the [Ar III] 7005 and 7751 Å lines. Since the line 7751 Å is located at the IR region of the spectra where the Goodman's CCD has more fringes, this can contribute to the higher errors found for Ar abundances. Another source of error is the ICF of Ar, whose uncertainty is much higher than the other elements, as noted by Delgado-Inglada et al. (2014). The S/O ratio is much more in agreement with the blue compact dwarf galaxy data. It is interesting to note that in our data we do not find the sulphur anomaly problem reported by other studies in the literature (see e.g. Henry et al. 2012). Since we have measured for most PNe of our sample the near-IR [S III] 9069 and 9532 Å lines, this reduces the uncertainties in S abundances, improving the accuracy of the abundances.

In Fig. 12, the N/O ratio is plotted against the He abundances. In the top panel, the abundances predicted by Karakas (2010) for stars of different initial masses are labelled with numbers indicating the masses used. Different colours and symbols are used to distinguish between each of the three different values of heavy element abundance Z. The majority of the observed points appear to lie between the curves for $Z = 0.02$ and 0.008, so that there is a general agreement between the predicted and observed abundances. However, some exceptions are noted: the PNe JaSt 23 and JaSt 52 show a very low abundance of He, which is not predicted by the models. Probably, neutral helium has an important contribution for the total helium abundance of these PNe. As discussed in Section 3.3, in the case of helium we opted not to use any ICF

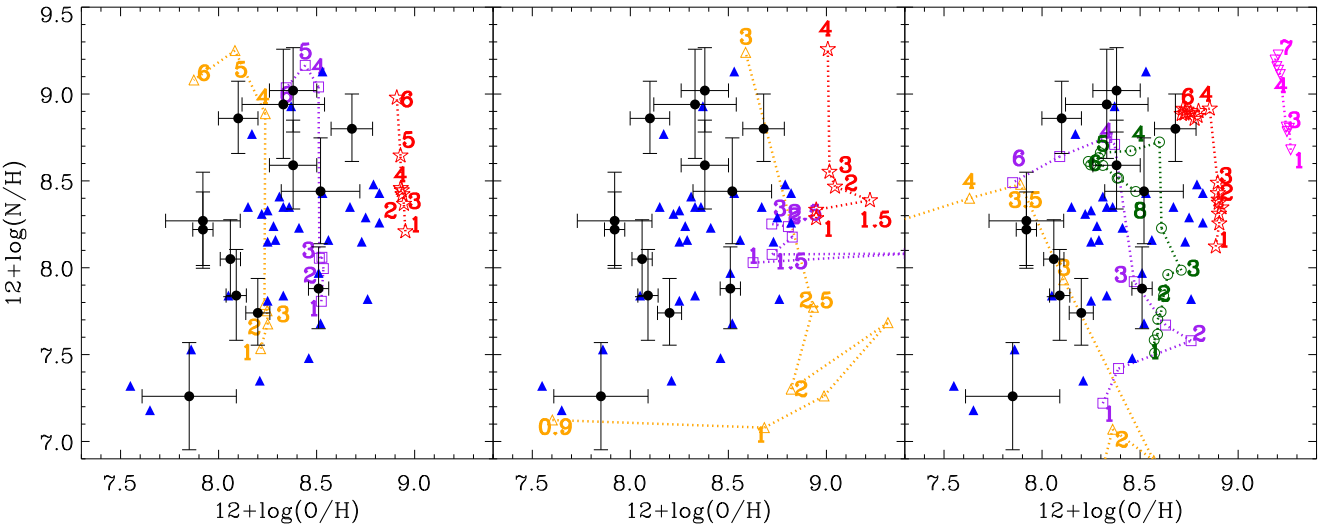

Figure 13. 12 + log (N/H) as a function of 12 + log (O/H). Left: comparison with the models from Karakas (2010); middle: comparison with the models from Miller Bertolami (2016); right: comparison with the models from Ventura et al. group. Symbols are as in Fig. 12.

since the relative populations of helium ions essentially depend on the effective temperature of the central star. Therefore, there is no reliable way to correct for neutral helium for these objects and the uncertainties are incorporated in the error bars for He abundances. As noted by García-Rojas et al. (2016), models by Karakas (2010) cannot predict the low N/O ratio (log(N/O) <-1.0) shown by some PNe. They pointed out two possible origins for this discrepancy. In the first one, the initial masses of the progenitor stars for these PNe should be lower than 1 $M_{\odot}$. However, this is unlikely since, using the Padova isochrones as revised by Mollá, García-Vargas & Bressan (2009), the mean lifetime for a star with 0.8 $M_{\odot}$ at solar metallicity is 15.8 Gyr and therefore higher than the expected age of the Universe. The second possibility is that stellar evolution models predict too large yields for N.

Since stellar nucleosynthesis models depend on the micro- and macrophysics adopted, it is also interesting to compare the data with different models in the literature. The Ventura et al. group provides a new generation of AGB stellar models that include dust formation in the stellar winds. During the core H-burning phase, the assumptions concerning the overshoot of the convective core lead to a less efficient dredge-up and to a lower threshold mass for the activation of the hot bottom burning than previous models in the literature. A detailed description of these models is given in Ventura et al. (2014a) for $Z = 0.004$, in Ventura et al. (2013) for $Z = 0.001$ and $M > 3$ $M_{\odot}$, and in Ventura et al. (2014b) for $Z = 0.001$ and $M < 3$ $M_{\odot}$. For $Z = 0.018$ and 0.04, the data were obtained from F. Dell'Agli and J. Garcia-Rojas (private communication). Hereafter we will call all these models as Ventura et al. group. Miller Bertolami (2016) provide AGB nucleosynthesis models including an updated treatment of the microphysics (radiative opacities and nuclear reaction rates) and description of the mixing processes and mass-loss rates that play a key role during the thermal pulses on the AGB phase. As a result, the new models lead to the occurrence of the third dredge-up for lower stellar masses. In Fig. 12, the results are compared with models from Miller Bertolami (2016) (middle panel) and Ventura et al. group (bottom panel). In this figure, we can observe a fair agreement between the data and the models. The different micro- and macrophysics adopted by each model change the progenitor masses at higher N/O ratios. The higher N/O ~ 0.6 from our data are compatible with progenitor masses of 3–4 $M_{\odot}$ in the case of the models from Miller Bertolami (2016) and of 5–6 $M_{\odot}$ in the case of the models from Karakas (2010) and Ventura et al. group. Note that JaSt 52 has very low abundances of O and a lower N/O ratio compared with the other PNe in our sample. Since neutral helium has an important contribution for this PN, the abundances for this object should be taken with caution.

The N/H abundances as a function of O/H abundances are displayed in Fig. 13. Most of our data are in agreement with the models by Karakas (2010) for higher metallicities. Exceptions are PNe JaSt 17 and JaSt 52 again (see discussion above) with a low O/H not predicted by the models at the given metallicities. In this figure, the predictions of the models are as expected: more massive stars produce larger amounts of N. In the case of the models by Miller Bertolami (2016), there is an offset towards higher O/H abundances compared with the data. The PNe in our sample PPA J1740−2708, PPA J1738−2800, PPA J1734−3004, JaSt 36 and JaSt 46 have N/H abundances compatible with models for initial stellar masses higher than 4 $M_{\odot}$.

An important difference between our sample and CCM10 is observed in Figs 12 and 13: in CCM10 some points are compatible with the lower metallicity model ($Z = 0.004$) by Karakas (2010) and also lower initial masses (<4 $M_{\odot}$). In our sample, a large fraction of PNe have abundances compatible with models at higher metallicities. Also, the superior limit for the initial masses depends on the model adopted. Considering the results from Miller Bertolami (2016), the PNe near the GC are compatible with stellar initial masses <3 $M_{\odot}$ for $Z = 0.001$. In the case of the models from Ventura et al. group for higher metallicities, the data are compatible with initial masses <6 $M_{\odot}$. On the other hand, Gesicki et al. (2014) using high-resolution imaging and spectroscopic observations of 31 compact PNe derived their central star masses. Post-AGB evolutionary models were used to fit the white dwarf mass distribution and initial–final mass relations were derived using white dwarfs in clusters. They obtained a mass distribution for GBPNe and found a mass limit of 2.5 $M_{\odot}$, which is lower than the masses obtained from the models in Fig. 12. However, we note that in Gesicki et al. (2014) the PN distribution in their fig. 9 shows that they explored a different region in the bulge since there are no PN within 2° from the GC.

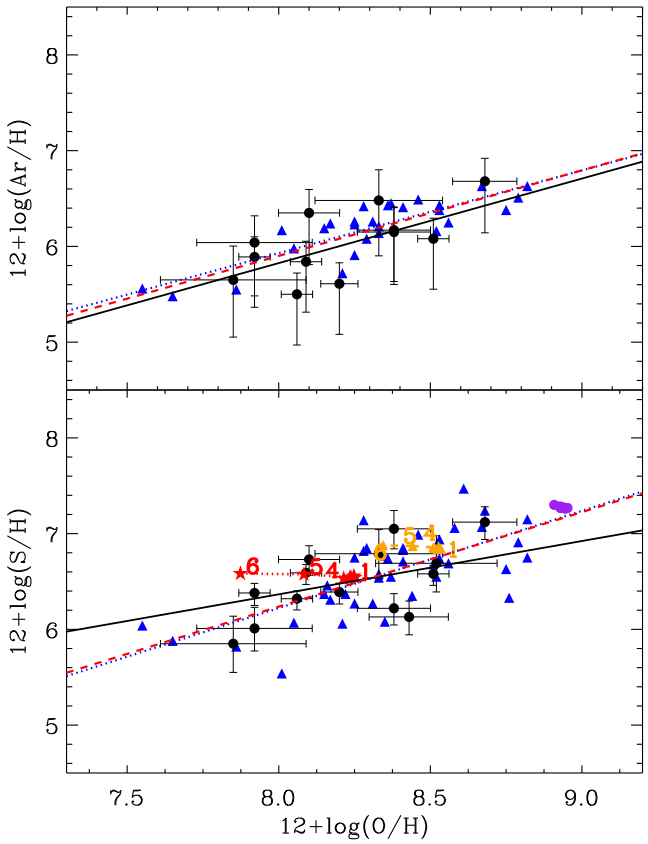

Figure 14. Top: 12 + log (Ar/H) versus 12 + log (O/H). Bottom: 12 + log (S/H) versus 12 + log (O/H). Symbols are as in the top panel of Fig. 12 for Karakas (2010) models. The lines are linear fits to the data: only PNe near the GC (black continuous line), only PNe from CCM10 (blue dotted line) and all the data (red dashed line).

The behaviour of Ar/H versus O/H and S/H versus O/H is presented in Fig. 14. A correlation is found for these elemental abundances for both samples. The linear Pearson correlation coefficients for CCM10 sample are 0.84 and 0.70 for Ar and S, respectively. The slopes of the linear fit are 0.86 and 1.02 for Ar and S, respectively. Considering only the GC sample, the correlation coefficients are 0.65 and 0.63 and the slopes 0.88 and 0.56, respectively. The low number of data points and also the uncertainties in the GC sample may wipe out the expected relations. However, considering all the data (this work + CCM10), the linear correlation coefficients are 0.79 and 0.69 for Ar and S, respectively. In this case, the slopes of the linear fit are 0.89 and 0.99. Therefore, there exist a linear relationship considering both samples. A detailed discussion of the correlations between neon, sulphur and argon abundances with oxygen in photoionized nebulae of the Local Group is given by Maciel, Costa & Cavichia (2017). The predictions of evolution models by Karakas (2010) at $Z = 0.004$, 0.008 and 0.02 are displayed in the graph for S/H versus O/H. Clearly, models show that S is not modified by stellar nucleosynthesis, independently of the initial stellar mass. On the contrary, O is expected to be modified in progenitor stars heavier than 4 $M_{\odot}$ at low-metallicity environments. In the case of Ar, the models by Karakas (2010) do not give predictions for these elements so that the abundances could not be compared with theoretical results.

The histograms of the abundances distributions for O/H, S/H, A/Hr and log (N/O) are shown in Fig. 15. We do not find important differences between the distributions of O/H, S/H and Ar/H comparing both samples. The average GC abundances of O/H, S/H and Ar/H are 0.13, 0.11 and 0.16 dex lower than the average values of the outer bulge sample, respectively. However, these differences are within the expected errors in the abundances. On the other hand, despite the low number of PNe in our sample, some important differences are evident in the histograms of log (N/O): the distribution for PNe near the GC is shifted for higher values compared with those from CCM10 data. The mean log (N/O) are −0.28 and 0.28 dex for CCM10 and GC samples, respectively. Therefore, the difference between both samples in log (N/O) is considerable (∼0.56 dex). Only for Ne the comparison cannot be made since, due to the high interstellar extinction in our spectra, we could not observe the [Ne III] 3869 Å and [Ne III] 3967 Å lines necessary to calculate the Ne elemental abundances. However, as alerted before, this result should be interpreted with some caution since, due to the high interstellar extinction in the direction of the GC, it is very difficult to define a metallicity-unbiased sample.

It is important to compare the results obtained in this paper with those from stars located near the GC. Ryde et al. (2016) have measured abundances of Mg, Si, Ca and Fe in 28 M-type giants in the GC region using high-resolution IR spectroscopy. Their data show a trend where the metallicity of the stars increases progressively as the stars are located closer to the GC. By means of high-resolution IR spectra, Cunha et al. (2007) observed a sample of cool stars within 30 pc from the GC. They obtained that [O/Fe] and [Ca/Fe] are enhanced by 0.2 and 0.3 dex, respectively, relative to the Sun Fe/H abundances. Their results pointed that the width of the [Fe/H] distribution in the GC is narrower than the one obtained for the older bulge population (outer bulge population). We note, however, that the data from Cunha et al. (2007) are located nearer to the GC than the PNe from our sample and the interpretation for the α-enhancement found in their sample might be different. Their interpretation is that the α-enhancement observed in cool stars near the GC might be due to an IMF weighted towards more massive stars or recent local type II supernova chemical enrichment within the central 50 pc of the Galaxy, or a mixture of bulge red-giant winds feeding the GC ISM. Regarding the results from other spiral galaxies, Florido et al. (2015) used a sample of nearby face-on disc galaxies with available SDSS spectra to derive chemical abundances of the ionized gas. Their results point to an enhancement of N/O in barred galaxies compared with non-barred galaxies. None the less, they do not find any difference regarding O/H. This difference in N/O and not in O/H in the centres of barred galaxies could be due to a different star formation efficiency in the inner parts of galaxies as a consequence of the influence of gas flows induced by the bars. Indeed, by means of a chemical evolution model, Cavichia et al. (2014) have simulated the gas flows induced by the Galactic bar and the influence on the Galactic bulge abundance distributions, finding no important differences. However, the star formation rate (SFR) is enhanced in the bulge when there is a radial gas flow towards the centre of the Galaxy. Nevertheless, the N/O distribution was not investigated in that work. In this work, we do not find evidence for important differences in the abundances of O/H, S/H and Ar/H in the GC PNe compared with those from the outer regions of the bulge. However, we do find evidence for higher N/O ratios in the GC sample, which is expected for more massive progenitor stars. The results of Figs 12, 13 and 15 point to recent SFR occurring in the GC, compared with the outer regions of the Galactic bulge. However, this result should be interpreted with

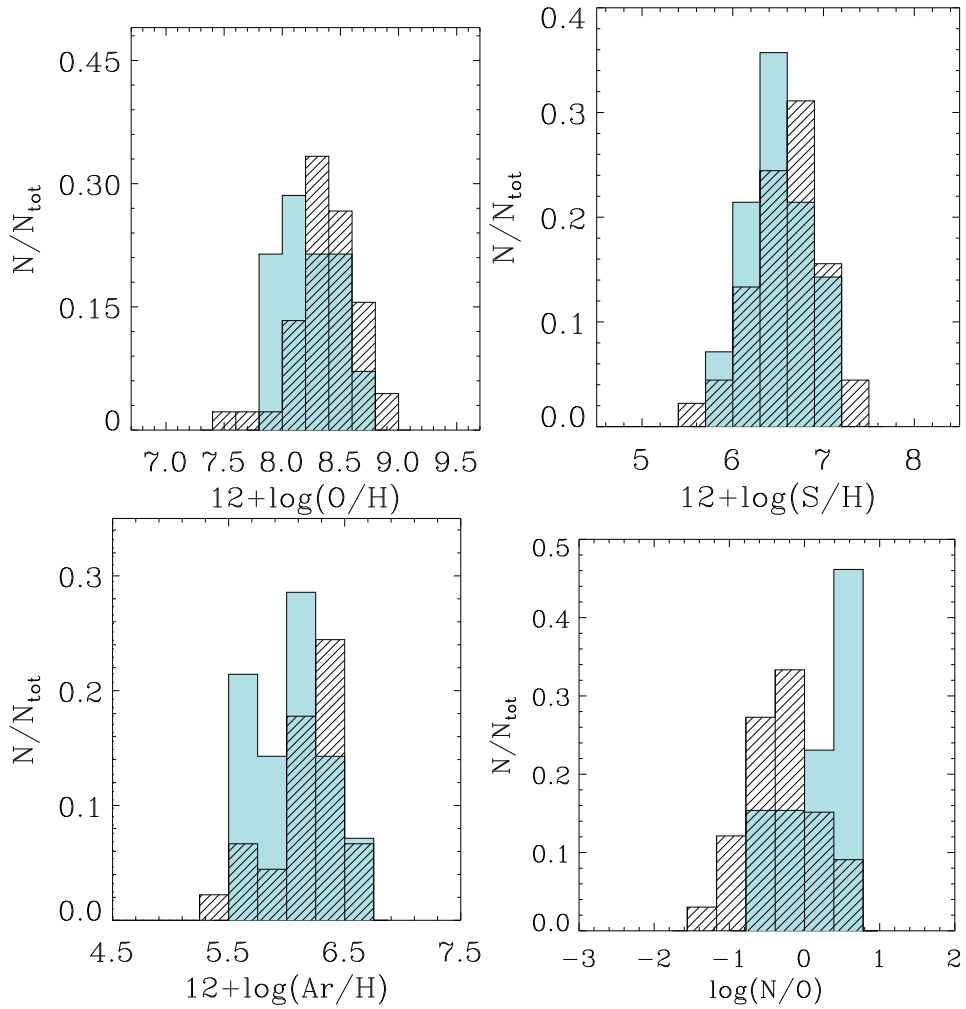

Figure 15. Abundances distributions (histograms) for 12 + log (O/H) (top left), 12 + log (S/H) (top right), 12 + log (Ar/H) (bottom left) and log (N/O) (bottom right). Filled histograms are the data from GBPNe near the GC and open histograms represent that from CCM10 (PNe from outer regions of the bulge).

some caution since, due to the high interstellar extinction in the direction of the GC, it is very difficult to define a metallicity-unbiased sample.

5 CONCLUSIONS

We have performed spectrophotometric observations with the 4.1-m SOAR (Chile) and the 1.6-m OPD/LNA (Brazil) telescopes to obtain physical parameters and chemical abundances for a sample of 17 PNe located within 2° of the GC. We derived chemical abundances for He, N, O, S and Ar. The results point to high obscured PNe, with $E(B-V)$ 2.3 on average. With such high extinction, no lines are seen in the blue part of the spectra, at wavelengths shorter than Hβ. We have implemented the new ICFs from Delgado-Inglada et al. (2014) for the elemental abundances determination and also the new He I emissivities from Porter et al. (2013). S abundances were derived using optical and NIR lines, reducing the uncertainties associated with S ICFs. The abundances predicted by Karakas (2010), Miller Bertolami (2016) and Ventura et al. group for stars of different initial masses and metallicity were used to constrain the masses and initial metallicity of the progenitor stars. An important difference between our sample near the GC and PNe located in the outer parts of the bulge is observed. In our previous work (CCM10, outer bulge region), some points are compatible with the lower metallicity model ($Z = 0.004$) by Karakas (2010) and also lower initial masses ($<4\,M_{\odot}$). In the PNe located near the GC, a large fraction of PNe have abundances compatible with models at higher progenitor masses. The results point to a considerable difference in log (N/O), and the PNe near the GC enhanced on average by ∼0.56 dex compared with PNe in the outer regions of the bulge. A higher N/O ratio is expected for more massive progenitor stars and may indicate recent episodes of star formation taking place at the GC, compared with the outer regions of the Galactic bulge.

A large percentage of PNe originated from stars formed in a high-metallicity environment is not expected in a bulge that purely originates from a gravitational collapse or by hierarchical merging of smaller objects. In this case, the formation process is generally fast and occurs earlier in the Galaxy formation process, before the present disc was formed. On the other hand, in bulges formed via disc instabilities (box/peanut bulges), the material that forms the bulge is originated by the rearrangement of the disc material through the secular evolution. Since the secular evolution causes a significant amount of star formation within the centre of galaxies

(Ellison et al. 2011), the stellar populations near the central parsecs of these galaxies are rejuvenating (Coelho & Gadotti 2011). In this scenario, a significant population of young stars is expected. However, a composite scenario with the possibility of a small classical bulge embedded within the box/peanut is not ruled out. The presence of multiple metallicity distribution within a bulge was noted in dissipative collapse models (e.g. Samland & Gerhard 2003) and also in bulges from cosmological simulations (Obreja et al. 2013). None the less, recently Ness et al. (2014) demonstrated that old stars are not exclusively linked to a classical bulge and the presence of young stars that are located close to the plane is expected for a bulge that has formed from the disc via dynamical instabilities. In summary, the results found in this paper collaborate to understand the chemical enrichment occurring at the Milky Way central regions. In spite of the results found, it is very difficult to define a complete sample in the GC region. Therefore, due to the low number of PNe and possible selection effects, more data of the same region as presented in this paper are necessary to draw firm conclusions about the chemical enrichment at the inner 2° of the Galactic bulge.

ACKNOWLEDGEMENTS

This work has been financially supported by the Brazilian agency FAPESP (Proc. 2007/07704-2, 2010/18835-3 and 2012/01017-1). We are grateful to the referee Dr Zijlstra for his comments and careful reading of the manuscript. OC would like to thank J. Garcia-Rojas and F. Dell'Agli for kindly providing the data from AGB nucleosynthesis models. This work is based on observations obtained at the Southern Astrophysical Research (SOAR) telescope, which is a joint project of the Ministério da Ciência, Tecnologia, e Inovação (MCTI) da República Federativa do Brasil, the U.S. National Optical Astronomy Observatory (NOAO), the University of North Carolina at Chapel Hill (UNC), and Michigan State University (MSU). Based upon observations carried out at the Observatório Pico dos Dias (OPD), LNA/MCTI - Brazil.

REFERENCES

Aver E., Olive K. A., Skillman E. D., 2010, J. Cosmol. Astropart. Phys., 5, 3
Bland-Hawthorn J., Gerhard O., 2016, ARA&A, 54, 529
Cahn J. H., Kaler J. B., Stanghellini L., 1992, A&AS, 94, 399
Cardelli J. A., Clayton G. C., Mathis J. S., 1989, ApJ, 345, 245
Cavichia O., Costa R. D. D., Maciel W. J., 2010, Rev. Mex. Astron. Astrofis., 46, 159 (CCM10)
Cavichia O., Costa R. D. D., Maciel W. J., 2011, Rev. Mex. Astron. Astrofis., 47, 49
Cavichia O., Mollá M., Costa R. D. D., Maciel W. J., 2014, MNRAS, 437, 3688
Chiappini C., Górny S. K., Stasińska G., Barbuy B., 2009, A&A, 494, 591
Clayton D. D., 1968, Principles of Stellar Evolution and Nucleosynthesis. McGraw-Hill, New York
Coelho P., Gadotti D. A., 2011, ApJ, 743, L13
Cuisinier F., Maciel W. J., Köppen J., Acker A., Stenholm B., 2000, A&A, 353, 543
Cunha K., Sellgren K., Smith V. V., Ramirez S. V., Blum R. D., Terndrup D. M., 2007, ApJ, 669, 1011
Delgado-Inglada G., Morisset C., Stasińska G., 2014, MNRAS, 440, 536
Eggen O. J., Lynden-Bell D., Sandage A. R., 1962, ApJ, 136, 748
Ellison S. L., Nair P., Patton D. R., Scudder J. M., Mendel J. T., Simard L., 2011, MNRAS, 416, 2182
Escudero A. V., Costa R. D. D., 2001, A&A, 380, 300
Escudero A. V., Costa R. D. D., Maciel W. J., 2004, A&A, 414, 211
Exter K. M., Barlow M. J., Walton N. A., 2004, MNRAS, 349, 1291
Fitzpatrick E. L., 1999, PASP, 111, 63
Fitzpatrick E. L., Massa D., 2009, ApJ, 699, 1209
Florido E., Zurita A., Pérez I., Pérez-Montero E., Coelho P. R. T., Gadotti D. A., 2015, A&A, 584, A88
Frew D. J., Parker Q. A., 2010, PASA, 27, 129
García-Rojas J., Peña M., Flores-Durán S., Hernández-Martínez L., 2016, A&A, 586, A59
Gesicki K., Zijlstra A. A., Hajduk M., Szyszka C., 2014, A&A, 566, A48
Gonzalez O. A., Rejkuba M., Zoccali M., Valenti E., Minniti D., Schultheis M., Tobar R., Chen B., 2012, A&A, 543, A13
Górny S. K., Chiappini C., Stasińska G., Cuisinier F., 2009, A&A, 500, 1089
Hamuy M., Walker A. R., Suntzeff N. B., Gigoux P., Heathcote S. R., Phillips M. M., 1992, PASP, 104, 533
Hamuy M., Suntzeff N. B., Heathcote S. R., Walker A. R., Gigoux P., Phillips M. M., 1994, PASP, 106, 566
Henry R. B. C., Kwitter K. B., Balick B., 2004, AJ, 127, 2284
Henry R. B. C., Kwitter K. B., Jaskot A. E., Balick B., Morrison M. A., Milingo J. B., 2010, ApJ, 724, 748
Henry R. B. C., Speck A., Karakas A. I., Ferland G. J., Maguire M., 2012, ApJ, 749, 61
Izotov Y. I., Stasińska G., Meynet G., Guseva N. G., Thuan T. X., 2006, A&A, 448, 955
Jacoby G. H., Van de Steene G., 2004, A&A, 419, 563 (JS04)
Karakas A. I., 2010, MNRAS, 403, 1413
Kingsburgh R. L., Barlow M. J., 1994, MNRAS, 271, 257
Maciel W. J., Lago L. G., Costa R. D. D., 2006, A&A, 453, 587
Maciel W. J., Costa R. D. D., Cavichia O., 2017, Rev. Mex. Astron. Astrofis., in press
Malkin Z., 2013, in de Grijs R., ed., Proc. IAU Symp. 289, Advancing the Physics of Cosmic Distances. Cambridge Univ.Press, Cambridge, p. 406
Milingo J. B., Kwitter K. B., Henry R. B. C., Souza S. P., 2010, ApJ, 711, 619
Miller Bertolami M. M., 2016, A&A, 588, A25
Miszalski B., Parker Q. A., Acker A., Birkby J. L., Frew D. J., Kovacevic A., 2008, MNRAS, 384, 525
Miszalski B., Acker A., Moffat A. F. J., Parker Q. A., Udalski A., 2009, A&A, 496, 813
Mollá M., García-Vargas M. L., Bressan A., 2009, MNRAS, 398, 451
Monreal-Ibero A., Walsh J. R., Westmoquette M. S., Vílchez J. M., 2013, A&A, 553, A57
Nataf D. M. et al., 2013, ApJ, 769, 88
Nataf D. M. et al., 2016, MNRAS, 456, 2692
Ness M., Debattista V. P., Bensby T., Feltzing S., Roškar R., Cole D. R., Johnson J. A., Freeman K., 2014, ApJ, 787, L19
Obreja A., Domínguez-Tenreiro R., Brook C., Martínez-Serrano F. J., Doménech-Moral M., Serna A., Mollá M., Stinson G., 2013, ApJ, 763, 26
Osterbrock D. E., Ferland G. J., 2006, Astrophysics of Gaseous Nebulae and Active Galactic Nuclei, 2nd edn. University Science Books, Mill Valley, CA
Parker Q. A. et al., 2006, MNRAS, 373, 79
Peyaud A. E. J., Boily C., Acker A., Parker Q., 2006, in Barlow M. J., Méndez R. H., eds, Proc. IAU Symp. 234, Planetary Nebulae in our Galaxy and Beyond. Cambridge Univ. Press, Cambridge, p. 485
Porter R. L., Ferland G. J., Storey P. J., Detisch M. J., 2012, MNRAS, 425, L28
Porter R. L., Ferland G. J., Storey P. J., Detisch M. J., 2013, MNRAS, 433, L89
Ryde N., Schultheis M., Grieco V., Matteucci F., Rich R. M., Uttenthaler S., 2016, AJ, 151, 1
Samland M., Gerhard O. E., 2003, A&A, 399, 961
Shaw R. A., Dufour R. J., 1995, PASP, 107, 896
Stanghellini L., Shaw R. A., Villaver E., 2008, ApJ, 689, 194
Stasińska G., Richer M. G., McCall M. L., 1998, A&A, 336, 667

Storey P. J., Zeippen C. J., 2000, MNRAS, 312, 813
Uscanga L., Gómez J. F., Suárez O., Miranda L. F., 2012, A&A, 547, A40
van Dokkum P. G., 2001, PASP, 113, 1420
Ventura P., Di Criscienzo M., Carini R., D'Antona F., 2013, MNRAS, 431, 3642
Ventura P., Criscienzo M. D., D'Antona F., Vesperini E., Tailo M., Dell'Agli F., D'Ercole A., 2014a, MNRAS, 437, 3274
Ventura P., Dell'Agli F., Schneider R., Di Criscienzo M., Rossi C., La Franca F., Gallerani S., Valiante R., 2014b, MNRAS, 439, 977
Wang W., Liu X.-W., 2007, MNRAS, 381, 669
Weiland J. L. et al., 1994, ApJ, 425, L81
Zijlstra A. A., Pottasch S. R., 1991, A&A, 243, 478
Zinn R., 1985, ApJ, 293, 424

SUPPORTING INFORMATION

Supplementary data are available at *MNRAS* online.

Table 4. Reddened fluxes relative to H β. $F(\mathrm{H}\,\beta)$ is in units of erg cm^{-2} s^{-1}.

Please note: Oxford University Press is not responsible for the content or functionality of any supporting materials supplied by the authors. Any queries (other than missing material) should be directed to the corresponding author for the article.

This paper has been typeset from a TEX/LATEX file prepared by the author.